Applied Acoustics 254 (2026) 111466

Contents lists available at ScienceDirect

Applied Acoustics

journal homepage: www.elsevier.com/locate/apacoust

Design and performance of the aeroacoustic wind tunnel of Politecnico di Milano

Gemma Bucherelli, Donato Grassi, Alberto Savino, Alberto Guardone, Alex Zanotti*

Politecnico di Milano, Dipartimento di Scienze e Tecnologie Aerospaziali, via La Masa 34, 20156, Milan, Italy

HIGHLIGHTS

- The new POLIMI-DAER facility targets the aeroacoustic challenges of Urban Air Mobility and multi-propeller systems.
- Aerodynamic tests confirm a flow uniformity within 1.4% and turbulence intensity as low as 0.14% at 30 m/s.
- The chamber features high-performance anechoic wedges providing a low acoustic cut-off frequency of 150 Hz.
- Validation with NACA 0012 airfoils confirms clear signal detachment from the facility's background noise floor.

ARTICLE INFO

Keywords:
Aeroacoustics
Wind tunnel
Qualification
Microphone
Airfoil

ABSTRACT

The present paper describes the design and qualification activity of the new anechoic wind tunnel built at the Aerodynamics Laboratory of the Department of Aerospace Science and Technology of Politecnico di Milano. The facility features a 4 m × 4 m × 4 m anechoic test chamber with a cut-off frequency of 150 Hz. The open-circuit wind tunnel is characterized by an open test section featuring a nozzle with a 0.7 m × 0.5 m outlet section and a collector with a 1.5 m × 1.5 m inlet section, for a maximum achievable speed of 42 m/s. The paper describes the main components employed for the design of the facility and the most relevant results obtained from the aerodynamic qualification of the jet flow and from the acoustic measurements performed in the test chamber. In particular, flow quality measurements showed a high degree of uniformity of the jet and enabled the identification of the jet's effective section along different planes past the nozzle outlet section. Moreover, hot-wire anemometry surveys enabled the identification of the turbulence intensity of the jet, having a value around 0.14% just behind the nozzle outlet section at operating conditions. Acoustic qualification results demonstrated low background noise levels, comparable to state-of-the-art academic wind tunnels of similar scale and performance. Furthermore, acoustic measurements conducted on benchmark cases, specifically a circular cylinder and a NACA 0012 airfoil, aligned with existing literature, confirmed the facility's suitability for aeroacoustic research in aeronautics. The facility fills a major national academic infrastructural gap, providing a strategic platform for the scientific advancement of the Italian aeroacoustics community, with testing capabilities specifically tailored to novel Advanced Air Mobility (AAM) configurations.

1. Introduction

The accurate characterization of airframe and propulsion noise requires specialized experimental facilities capable of decoupling the aeroacoustic signature of a model from the environmental noise floor. Anechoic wind tunnels are specifically engineered to provide a high-quality, low-turbulence flow while maintaining an environment conducive to high-fidelity acoustic measurements. Unlike conventional aerodynamic tunnels, these facilities must address two simultaneous challenges, i.e., the generation of a stable flow field and the suppression of acoustic reflections that could contaminate the pressure transducers' signals. A critical requirement for the validity of aeroacoustic data is the Signal-to-Noise Ratio (SNR). According to the criteria established by Soderman [1], a minimum SNR of 10 dB is necessary to ensure that the measured acoustic pressure fluctuations are representative of the model's self-noise rather than the facility's background noise. This threshold is particularly challenging to maintain at high flow velocities, where the noise from the wind tunnel's drive system and the interaction

* Corresponding author.
Email address: Alex.Zanotti@polimi.it (A. Zanotti).

https://doi.org/10.1016/j.apacoust.2026.111466
Received 24 March 2026; Received in revised form 6 July 2026; Accepted 9 July 2026
Available online 16 July 2026

Notation

A nozzle outlet section area [m^2]
AAM Advanced Air Mobility
A_c cross-sectional area of the anechoic chamber [m^2]
A_{coll} cross-sectional area of the collector [m^2]
d circular cylinder diameter [m]
d_{hw} hot wire diameter [m]
D_h hydraulic diameter [m]
eVTOL electric Vertical Take-Off and Landing aircraft
f frequency [Hz]
f_S sampling frequency [Hz]
F.S. differential pressure sensor full-scale range [Pa]
h nozzle outlet section height [m]
H anechoic test chamber height [m]
H_{coll} collector height [m]
K_i non-dimensional pressure loss coefficient in component i [-]
L anechoic test chamber length [m]
N spectral scaling exponent [-]
NRC Noise Reduction Coefficient [-]
OASPL Overall Averaged Sound Pressure Level [dB]
PSD Power Spectral Density of pressure fluctuations [Pa^2/Hz]
r distance from the nozzle outlet center [m]
Re_{d_s} wire-based Reynolds number for screens [-]
Re_{hw} wire-based Reynolds number for hot wire probe [-]
RMS Root Mean Square
R_w weighted sound insulation index [dB]
SNR Signal-to-Noise Ratio [dB]
SPL Sound Pressure Level [dB]
St Strouhal number [-]
S_{uu} Power Spectral Density of u [$(m/s)^2$/Hz]
TI Turbulence Intensity [%]
u streamwise velocity component [m/s]
v spanwise velocity component [m/s]
UAM Urban Air Mobility
V reference velocity [m/s]
V_∞ freestream velocity [m/s]
w nozzle outlet section width [m]
W anechoic test chamber width [m]
W_{coll} collector width [m]
$X-Y-Z$ reference system
α angle of attack [deg]
α_w sound absorption coefficient
β screen porosity [-]
δ shear layer thickness [m]
Δp_i pressure losses in component i [Pa]
θ microphone polar angle [deg]
μ dynamic viscosity [kg/(ms)]
ρ air density [kg/m^3]
σ spreading rate [-]
σ_v standard deviation of the streamwise velocity component [m/s]

of the flow with the nozzle exit can become dominant. To achieve these conditions, the test sections of aeroacoustic tunnels are typically located in anechoic chambers, where internal walls are lined with anechoic wedges constructed from sound-absorbent materials, to create an acoustic far-field environment, preventing sound reflection into the test region while absorbing shorter wavelengths.

Historically, the development of these facilities has transitioned from modified hard-wall tunnels to purpose-built open-jet configurations. The open-jet layout is often preferred for aeroacoustics because it allows the placement of microphones outside the flow, thus avoiding the pseudo-sound associated with the turbulent boundary layer of a closed wall [2,3]. However, this introduces the challenge of the shear layer, which can refract acoustic waves—a phenomenon that requires appropriate analytical or numerical corrections, such as those proposed by Amiet [4]. The design of the collector also plays a pivotal role in maintaining flow stability; its geometry must be carefully optimized to avoid flow separation and unsteady behavior, which can compromise both aerodynamic and acoustic measurements [5].

Over the past two decades, the field has seen a significant surge in the construction and upgrading of aeroacoustic infrastructures. The automotive industry has historically spearheaded the development of large-scale facilities, leveraging substantial capital investments. Conversely, academic institutions have focused on developing more compact and versatile layouts. A review of the most significant layouts reveals a variety of specialized approaches. The ISVR anechoic wind tunnel at the University of Southampton [3] is renowned for its high-speed capabilities, reaching Mach 0.3 while maintaining remarkably low cut-off frequencies. Similarly, the High-Speed Aeroacoustic Wind Tunnel at Carleton University [6] is characterized by a comparable design approach, enabling high-speed operation with low background noise, and the investigation of boundary layer noise under controlled conditions.

The design of the settling chamber and the contraction ratio are equally critical for ensuring a low-turbulence core flow. Aeroacoustic wind tunnel designs typically employ high contraction ratios and multiple fine-mesh screens to achieve very low turbulence levels required for accurate aeroacoustic measurements. An example of such design philosophy can be found in German research facilities, including configurations developed at the Technical University of Berlin, which follow these general principles (see, e.g., [7]).

Flexibility is also a key design driver, as demonstrated by the Virginia Tech facility [8], which features a hybrid test section that can be reconfigured between hard-wall and anechoic arrangements, thus allowing the selection of the most suitable configuration depending on aerodynamic or aeroacoustic measurements. As a matter of fact, when designing a wind tunnel dedicated to aeroacoustic research, a fundamental architectural choice involves selecting between an open-section (open-jet) and a closed-section configuration. Both layouts present inherent strengths and weaknesses that significantly impact the quality of both aerodynamic and acoustic measurements, as discussed by Kröber [9] and Amaral et al. [10]. In particular, closed-section wind tunnels offer a highly controlled testing environment characterized by excellent flow uniformity and the absence of shear-layer instabilities or acoustic pumping phenomena. From an acoustic standpoint, they eliminate the problem of sound wave refraction since the acoustic path from the source to the microphone does not cross any flow boundaries. However, closed configurations suffer from severe acoustic reflections off the solid walls, which can contaminate the acoustic field. Furthermore, the boundary layer developing along the walls generates high levels of background noise and positioning microphones directly inside the flow introduces parasitic aerodynamic noise on the sensors unless complex wall-flush or Kevlar-wall solutions are implemented. On the other hand, open-section configurations are widely preferred for aeroacoustic testing because they allow microphones to be placed outside the energetic flow, inside an anechoic or semi-anechoic chamber. This layout drastically reduces the aerodynamic background noise on the sensors and minimizes acoustic reflections. Nevertheless, as previously outlined, the open-jet boundary introduces a turbulent shear layer between the moving flow and the stagnant air of the chamber. This shear layer scatters and refracts the acoustic waves traveling from the model to the external microphone array. Additionally, open-jets are susceptible to low-frequency pressure fluctuations and facility buffeting at high velocities.

The physical scale of the facility also remains a critical factor. The NASA Anechoic wind tunnel LSAWT [11] boasts the largest test sections, as small scales make it complex to accurately simulate aspects of powered-lift aircraft aerodynamics and to achieve proper helicopter-rotor Reynolds number, advance ratio, and Mach numbers simultaneously. The large test section also facilitates measurements in the acoustic far field, avoiding measurement distortion and increasing the distance between the model and the lateral walls, thus minimizing boundary layer noise interference. Similarly, the AUDI wind tunnel layout [12] features a large test section capable of accommodating both full-scale cars and scaled models, thereby avoiding aerodynamic simplifications and data rescaling. These characteristics make it a reference and check tool for all aero-acoustic tests requiring free-field conditions and low background noise levels. Furthermore, it features a moving belt, enabling aerodynamic and aeroacoustic underbody optimizations.

The rapid evolution of Urban Air Mobility (UAM) has shifted the research focus in aeronautical field toward complex aeroacoustic interactions inherent in multi-rotor and distributed electric propulsion (DEP) systems. Recent experimental campaigns have highlighted that the acoustic signature of such vehicles is dominated by unsteady phenomena. For instance, Zawodny et al. [13] at the NASA Langley LSAWT conducted studies on wing-propeller systems, identifying how leading-edge vortex ingestion significantly alters far-field directivity. Similarly, Celik et al. [14] recently utilized the University of Bristol facility comprising a large anechoic test chamber and a temperature controlled closed-circuit wind tunnel with an open test section, to characterize overlapping propellers, demonstrating noise elevations of up to 18 dB due to blade-vortex interactions (BVI). These findings are complemented by recent works within the GARTEUR Action Group HC/AG-26 framework [15–17], involving different European research centers and universities in a collaborative study aimed at investigating the acoustic and aerodynamic performance of interacting propeller configurations, i.e., tandem and coaxial, with a focus on the code-to-code comparison of aeroacoustic solvers with different levels of fidelity.

To address these challenges and bridge a critical gap by establishing a unique facility within the Italian academic landscape, a new anechoic wind tunnel has been designed and constructed at the Department of Aerospace Science and Technology (DAER) of Politecnico di Milano (POLIMI) to deliver performance that is fully comparable to the current state-of-the-art facilities in Europe. Developed within the framework of the MOST - Sustainable Mobility National Research Center (funded by the EU Next-Generation EU/PNRR), this facility is specifically tailored for investigating interactional aeroacoustics on scaled multi-propeller configurations [18]. This new wind tunnel represents a unique facility in the Italian academic environment and is part of the excellence research center on AAM developed at POLIMI-DAER.

The present paper describes the design methodology of the facility and presents the results of its aerodynamic and acoustic qualification aimed at evaluating the aerodynamics and acoustic performance of the new wind tunnel, particularly focusing on the identification of the effective jet section usable for the tests and the characterization of background noise levels. In particular, this activity resembled the workflow described by Mayer et al. [19] for the qualification of the University of Bristol wind tunnel, representing a comparable facility in terms of dimensions and performance. Furthermore, methodological guidance and inputs for acoustic performance comparison in the qualification process was drawn from the Brandenburg University of Technology (Cottbus) [20], as well as from the academic open-jet facilities at the University of Adelaide [21] and the University of Florida [22]. In addition, following the approach of Mayer et al. [19], this study evaluates acoustic measurements on benchmark test cases, specifically a circular cylinder and a NACA 0012 airfoil. These tests assess the facility's capability to characterize the acoustic emissions of standard bluff and lifting bodies, which are fundamental to aeroacoustic research.

2. Wind tunnel design

The design of the POLIMI anechoic wind tunnel was constrained by the space allocated within the Aerodynamics Laboratory of POLIMI-DAER, comprising a volume 16.9 m long, 7.5 m wide, and 5.8 m high. This spatial constraint necessitated an open-circuit layout and determined the dimensions of the anechoic test chamber. At the early design stage, specific technical objectives were defined to further guide the dimensioning of the facility. In particular, the wind tunnel has to reach the target velocity of 30 m/s, representing a realistic value in the cruise flight condition of an eVTOL aircraft [23], a meaningful test case for the scope of the present facility, with a turbulence intensity level below 0.5% at nozzle outlet section. From the acoustic point, the target was to have a background noise level comparable to that of state-of-the-art existing aeroacoustic wind tunnels with similar dimensions at the target speed of 30 m/s, such as the one at University of Bristol, for which the work by Mayer et al. [19] reports an overall sound pressure level around 59 dB.

The layout of the POLIMI-DAER anechoic wind tunnel is presented in Fig. 1, which shows a three-dimensional render sectioned by a horizontal plane to highlight internal features such as turning vanes and silencers. A silenced duct serves as the inlet for the open circuit (Part A), followed by a corner duct equipped with turning vanes (Part B) and a settling chamber containing a turbulence screen and honeycomb section. The contraction nozzle (Part C), with an outlet section of 0.7 m × 0.5 m, protrudes 1 m into the anechoic test chamber (Part D). This fully anechoic

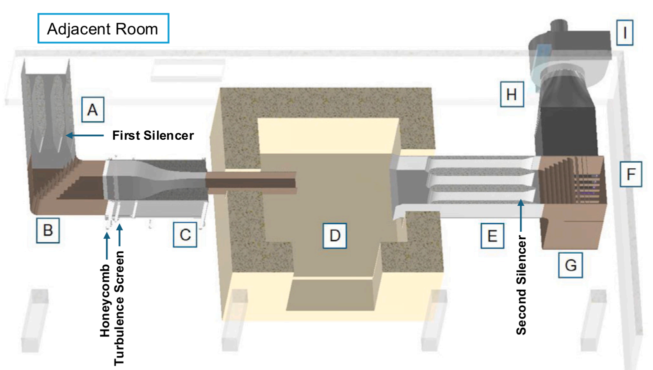

(a) 3D Rendering.

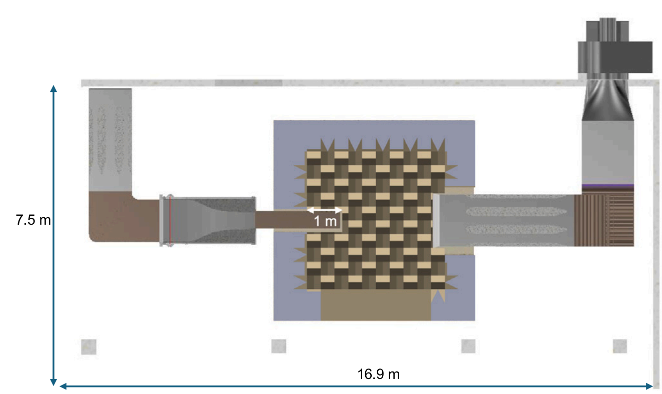

(b) Floor View.

Fig. 1. POLIMI-DAER anechoic wind tunnel layout: (A) silenced inlet duct, (B) first corner with turning vanes, (C) contraction nozzle (0.7 m × 0.5 m section), (D) anechoic chamber, (E) silenced collector (1.5 m × 1.5 m section), (F) second corner with turning vanes, (G) third corner with turning vanes, (H) rectangular-to-round section change duct, (I) centrifugal fan.

chamber, characterized by a cut-off frequency of 150 Hz, has an internal volume of 4 m × 4 m × 4 m, net of the acoustic wedges covering the walls. The free jet is collected by a silenced collector duct with a 1.5 m × 1.5 m bell-mouth inlet section (Part E). The collector duct is followed by two corners equipped with turning vanes (Parts F and G). A rectangular-to-round transition duct (Part H) passes through a concrete wall to channel the flow to the centrifugal fan (Part I) located in an adjacent room. The flow within the open-jet wind tunnel is generated by drawing air from the adjacent room through the bell-mouth inlet of the collector.

All ducts were designed to be airtight, and their internal surfaces (Parts A, B and E to F) were acoustically treated with mineral wool covered by galvanized expanded steel sheets, in accordance with classical porous liner treatment principles (see, e.g., [24,25]). This treatment provides acoustically absorptive boundary conditions and minimizes internal sound reflections within the duct system. The mineral wool provides the primary sound absorption mechanism through viscous and thermal dissipation within the porous medium, while the perforated steel sheet acts as a protective facing, ensuring structural integrity and defining a controlled acoustic impedance at the boundary. This combination reduces reflection coefficients over a broad frequency range, thereby limiting the formation of standing waves and preventing contamination of the measured acoustic field by duct-borne resonances. Similar acoustic wall treatments are commonly implemented in aeroacoustic measurement facilities to control internal reflections and reduce background noise contamination, as demonstrated in the work of Bento et al. [26] for wind tunnel applications. Such design strategies are consistent with established practices in low-noise aeroacoustic wind tunnels, where the mitigation of duct-borne noise and reflection effects is critical to ensure measurement fidelity [12,19]. In particular, acoustic wall treatments are based on the use of 50 mm thickness FIBRANgeo B-570 stone wool panels manufactured from bio-soluble mineral fibers, with 75 kg/m^3 nominal density, protected by 2 mm galvanized expanded steel sheets with an open area ratio of approximately 54%. This perforated sheet metal ensures complete acoustic transparency [27]. The basic prefabricated stone wool modules are then assembled in dual-layer configurations to reach the total insulation thickness of the wall (see hex pattern in Fig. 10). According to the manufacturer datasheet,[1] the stone wool module exhibits a sound absorption coefficient $\alpha_w = 1$ (EN ISO 11654) and a Noise Reduction Coefficient NRC = 1 (ASTM 423) for thickness ≥ 50 mm, indicating very high absorption performance in the mid-to-high frequency range.

All the corners along the facility feature turning vanes consisting of a 90° arc with a 200 mm radius and an 80 mm straight trailing edge extension, manufactured from 3 mm thick steel plates with chamfered edges. The primary design features of the main wind tunnel components are described in the following subsections.

2.1. Anechoic test chamber

The design of the airtight anechoic chamber features external dimensions of 5.94 m × 5.94 m × 5.53 m, including the surrounding acoustic walls, as shown in the drawings in Fig. 2. The acoustic walls are made of FIBERMET EVO 100 high-performance, insulated sandwich metal panels designed for wall cladding and partition applications, featuring a nominal thickness of 100 mm. The panel consists of two 0.6 mm thick galvanized steel facings auto-bonded to a 75 kg/m^3 structural stone wool core with oriented fibers running perpendicular to the metal skins. According to the manufacturer's datasheet,[2] a single 100 mm thick panel achieves a certified weighted sound insulation index of $R_w = 34.7$ dB and a sound absorption coefficient $\alpha_w = 0.9$. A multi-layer panel configuration with a total thickness of 0.41 m (see Fig. 2) provides a sound insulation value of 62 dB between the internal and external volumes,

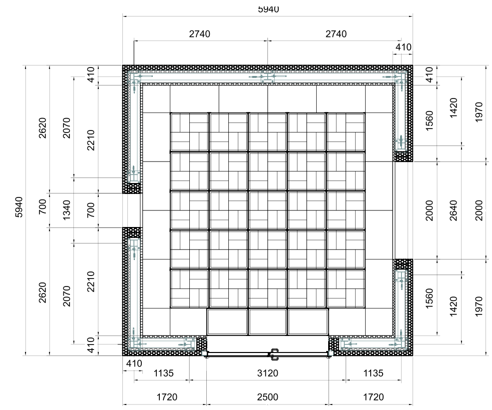

(a) Top View

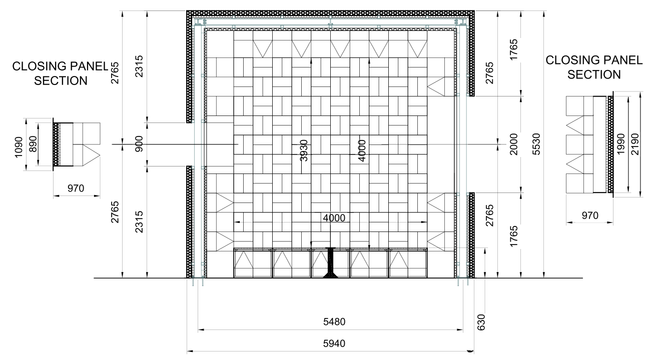

(b) Lateral view

Fig. 2. Anechoic chamber technical drawings (dimensions in mm).

evaluated by dedicated tests performed by the anechoic chamber manufacturer Bosco Italia[3] in accordance with UNI EN ISO 143-3:2006 and UNI EN ISO 717-1:2001 testing procedures. The central module of the external structure features a 3.2 m wide lateral door to allow staff access to the test area, facilitating model adjustments during measurements via an open-mesh raised floor. The lateral modules constituting the external walls are reinforced with tie rods to enhance stiffness and support the 0.9 m × 0.7 m and 2 m × 2 m openings designated for the installation of the final portion of the contraction nozzle and the collector, respectively. To prevent acoustic reverberation, all internal walls of the chamber are covered with wedges made of 50 mm thick ACUPOL White[4] polyester fiber panels (density 40 kg/m^3) exploiting a sound absorption coefficient of $\alpha_w = 0.8$. The design and installation follow the pattern and dimensions shown in Fig. 3, where two sets of orthogonally positioned wedges improve noise diffraction, directing sound waves along a maze-like path to enhance interaction with the absorbing material. Additionally, the internal surface of the lateral door is lined with the same material to prevent external noise infiltration. The anechoic chamber is certified for anechoic measurements down to 150 Hz, which was experimentally verified during the facility's commissioning phase. The acoustic qualification was performed in accordance with ISO 3745 standards using an omnidirectional dodecahedron sound source and systematic microphone measurements.

To ensure both aerodynamic validity and acoustic free-field conditions, the geometric scaling between the open-jet nozzle exit area (A) and the cross-sectional area of the anechoic chamber (A_c), net of the

[1] https://fibranit.b-cdn.net/wp-content/uploads/sites/2/2024/05/Technical-Data-Sheet-FIBRANgeo-B-570.pdf.
[2] https://www.isolpack.com/wp-content/uploads/fibermet.pdf.
[3] https://boscoitalia.it/.
[4] https://www.acusticaindustriale.it/documenti/prodotti/en/1cea5220-4.pdf.

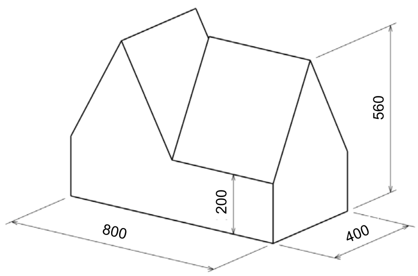

Fig. 3. Installation pattern of the wedges used in the anechoic test chamber (dimensions in mm).

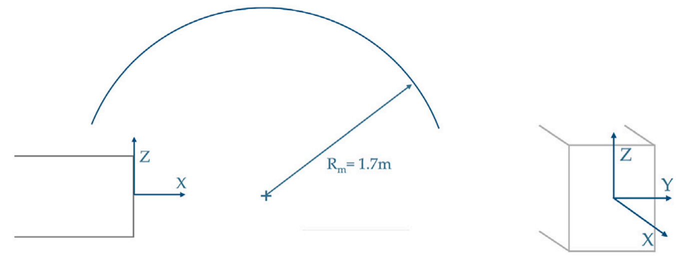

Fig. 4. Scheme of the microphones' arc fixed to the anechoic test chamber ceiling and reference system with origin at the center of the nozzle outlet section.

acoustic wedges, has to be taken into account as a design constraint. Indeed, this scaling is dictated by a coupled balance between aerodynamic constraints (i.e., preventing jet deflection, excessive shear layer interaction, or flow recirculation) and acoustic requirements (i.e., ensuring far-field microphone placement outside the hydrodynamic near-field and proper wave attenuation at the minimum design cut-off frequency), while satisfying the free-field propagation requirements down to the design cut-off frequency according to ISO 3745. The guideline used in the present activity was to follow recommended practices in modern small-to-medium scale academic aeroacoustics facilities design by taking into account the results of a cross-comparison of the available scaling metrics of prominent state-of-the-art aeroacoustic wind tunnels from small to large-scale industrial facilities referenced in literature. Table 1 summarizes the main geometric characteristics of these sample facilities and highlights the area ratio A/A_c to be compared with the metric used in the present facility.

The data analysis reveals a clear sizing trend. Indeed, while state-of-the-art aeroacoustic facilities with small-to-medium sizes reveal this area ratio limited to under 4%, in medium to large facilities, the area ratio slightly increases up to about 9% due to the massive economic and structural constraints of building larger acoustic enclosures. In the present work, our facility features a geometric area ratio of about 2%, thus well within the trend identified from established international benchmarks, confirming that the current architecture satisfies both the aerodynamic free-expansion constraints and the far-field acoustic measurement criteria required for high-fidelity aeroacoustic testing.

Far-field noise measurements are performed using two microphone arrays mounted on separate metallic arcs. A fixed arc, treated with sound-absorbing material, is ceiling-mounted and aligned with both the nozzle center point and the freestream direction. This fixed structure supports an array of eleven equally spaced microphones spanning 126°, with diaphragms positioned at a 1.7 m radius relative to the center of the anechoic chamber. A scheme showing the microphone arc positioning fixed to the anechoic test chamber ceiling is presented in Fig. 4, together with the reference system (X,Y,Z) used to identify the microphone positions in the acoustic qualification. The anechoic test chamber could also be equipped with a secondary twin movable arc, mounted on a wheeled aluminum profile structure, to allow dedicated far-field acoustic measurements around the model position along the jet. This arc is capable of rotation about the centerline axis, allowing for polar measurements along either vertical or longitudinal planes relative to the model. The microphone array utilizes 1/4" GRAS 40PL-10 CCP sensors, with detailed specifications provided in Table 2.

Table 2
Specifications of GRAS 40PL-10 CCP microphone.

Dynamic range	Frequency response	Sensitivity	Uncertainty
32–135 dB(A)	10 Hz–20 kHz	9 mV/Pa	±2 dB

A picture of the anechoic chamber, also showing the far-field microphone setup on the fixed arc mounted on the ceiling, is presented in Fig. 5.

2.2. Contraction nozzle and settling chamber

To reduce facility costs, the contraction nozzle, which features a contraction ratio of 6.25, and settling chamber were repurposed from a decommissioned open-circuit wind tunnel at the POLIMI-DAER Aerodynamics Laboratory, a system with a documented history in research activities [35]. The component was constructed via the backward extrusion of a solid box, supported by an aluminum profile structure to facilitate precise mounting and alignment with the inlet duct and the primary corner. The nozzle geometry was designed following the guidelines proposed by Barlow et al. [5] Chap. 3.4, which are widely adopted in low-turbulence wind tunnel design to ensure a sufficiently uniform flow, with smooth acceleration and minimal boundary layer growth. In

Table 1
Geometric scaling metrics of anechoic test chamber sections with respect to nozzle exit area in state-of-the-art aeroacoustic wind tunnels.

Wind Tunnel Facility	Nozzle Dim. $w \times h$ [m]	Nozzle Area $A = w \times h$ [m^2]	Chamber Dim. $W \times H \times L$ [m]	Chamber Area $A_c = W \times H$ [m^2]	Area Ratio A/A_c [%]
Southampton [3]	0.15×0.45	0.0675	$5.25 \times 5.25 \times 5.25$	27.56	0.24
Bristol [19]	0.5×0.775	0.3875	$4 \times 3.3 \times 6.7$	13.2	2.9
Cottbus [20]	⌀ 0.35	0.0962	$1.5 \times 1.5 \times 2.5$	2.25	4.2
Penn State [28]	0.6×0.6	0.36	$6 \times 2.8 \times 5$	16.8	2.1
AWB-DLR [29]	0.8×1.2	0.96	$8 \times 8 \times 7.94$	64	1.5
Adelaide [30]	0.275×0.075	0.02	$1.4 \times 1.4 \times 1.6$	20.6	1.02
Univ. of Florida [22]	1.12×0.74	0.83	$5 \times 2.3 \times 5.5$	11.5	7.2
Florida State [31]	1.219×0.94	1.145	$4.5 \times 2.7 \times 4.8$	12.15	9.4
ISAE-SUPAERO [32]	1.8×1.8	3.24	$8 \times 7 \times 7$	56	5.78
DTU (Paul la Cour) [33]	3×2	6	$9 \times 9.5 \times 11$	85.5	7
DNW-LLF [34]	8×6	48	$30 \times 30 \times 26$	900	5.3
Politecnico di Milano	0.5×0.7	0.35	$4.0 \times 4.0 \times 4.0$	16	**2.19**

Fig. 5. Internal view of the anechoic test chamber of the POLIMI-DAER anechoic wind tunnel.

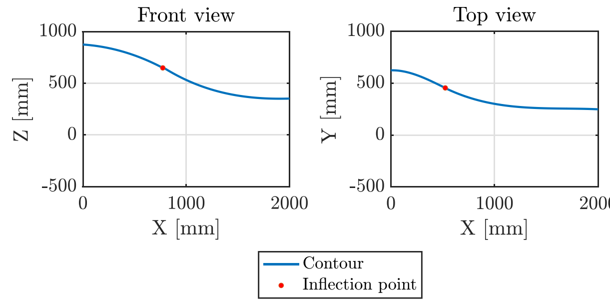

Fig. 6. Frontal and top views of the contraction nozzle contour.

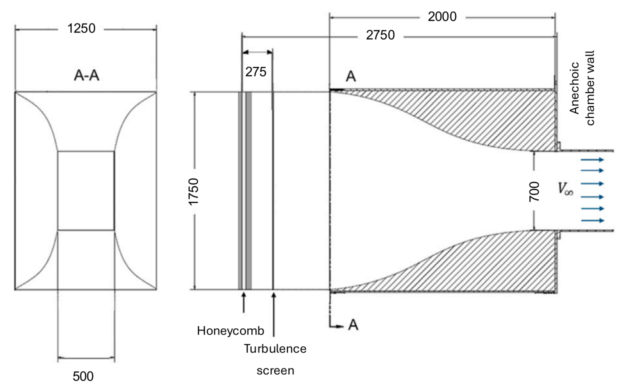

Fig. 7. Frontal and lateral views of the contraction nozzle and settling chamber layouts (dimensions in mm, hatched pattern indicates solid filled material).

particular, its contour was defined to provide a gradual variation of the cross-sectional area, avoiding abrupt curvature changes and inflection points that could promote flow separation, which also causes flow-induced noise, detrimental for aeroacoustic applications. The geometry of the contraction nozzle is defined by two orthogonal planar profiles corresponding to the front and top views of the convergent section (see Fig. 6). Each profile can be approximated using a piecewise cubic interpolation, subdividing the domain at the location of maximum curvature variation, identified through a curvature-based criterion, which corresponds to the inflection region of the geometry. This approach allows representing each nozzle contour as two third-order polynomial functions defined upstream and downstream of the inflection point, ensuring a smooth and continuous description of the wall profile, according to the following equations,

$$Z(X) = \begin{cases} -2.2284\cdot 10^{-8}X^3 - 2.7048\cdot 10^{-4}X^2 - 6.9840\cdot 10^{-2}X + 875.2101, & X \leq 773.18 \\ -7.3276\cdot 10^{-8}X^3 + 5.7396\cdot 10^{-4}X^2 - 1.3891X + 1420.8209, & X > 773.18 \end{cases} \tag{1}$$

$$Y(X) = \begin{cases} 6.7196\cdot 10^{-7}X^3 - 1.0224\cdot 10^{-3}X^2 + 2.7103\cdot 10^{-2}X + 624.6169, & X \leq 524.55 \\ -1.1651\cdot 10^{-7}X^3 + 5.9155\cdot 10^{-4}X^2 - 1.0117X + 837.9324, & X > 524.55 \end{cases} \tag{2}$$

The outlet section of the extruded box is positioned against the outer wall of the anechoic chamber. This is extended by a 0.7 m × 0.5 m constant-section duct, which protrudes 1 m into the anechoic test chamber (as illustrated in Fig. 1). To minimize acoustic interference and ensure the integrity of the anechoic environment, the protruding section of the duct is externally clad with 50 mm thick acoustic absorbing foam sheets.

The settling chamber, 0.75 m long and featuring a 1.25 m × 1.75 m cross-section, is equipped with two metallic frames designed to support a flow-straightening honeycomb and a turbulence-reduction screen (see Fig. 7). The choice of employing a single screen results from a compromise between achieving adequate flow quality and maintaining a sufficient distance between the last screen and the nozzle inlet section (approximately 0.35 m), which is required to allow proper turbulence decay and flow homogenization downstream of the flow conditioning devices, in accordance with classical wind tunnel design guidelines [5,36]. Such a development length is necessary to ensure the dissipation of residual disturbances generated by the screen and to promote a sufficiently uniform, low-turbulence flow at the contraction inlet, as commonly observed in compact low-speed wind tunnel designs [37].

The 80 mm thick honeycomb section is composed of hexagonal cells with a side length of 6.5 mm. This cell size provides effective suppression of lateral velocity components while maintaining a sufficiently high open-area ratio to limit pressure losses. The thickness of 80 mm ensures an adequate length-to-cell-size ratio, within recommended ranges, which is typically required to properly straighten the flow by suppressing lateral velocity components and reducing large-scale swirl structures, while containing pressure losses and overall dimensions.

The turbulence screen is constructed as a plain-weave mesh using stainless steel wires with a diameter of 0.8 mm and a mesh opening of 2.8 mm, providing an appropriate balance between turbulence attenuation efficiency and acceptable pressure loss. This geometry yields a porosity of $\beta = 0.604$, which satisfies the fundamental criterion of $\beta > 0.57$ [36] to prevent jet coalescence and spatial flow non-uniformities. Based on a test section design velocity of $V_\infty = 30$ m/s and a contraction ratio of 6.25, the reference velocity within the settling chamber yields a wire-based Reynolds number of approximately $Re_{d_s} = 250$. According to Groth and Johansson [38], at this Reynolds number, the screen operates in a stable subcritical regime, where vortex shedding occurs behind the individual wires. In this condition, the turbulence produced by the screen itself is dominated by screen-generated small scales within the initial near-wake region, after which a rapid power-law decay toward very low background turbulence levels occurs. The screen is therefore used as an effective flow-conditioning element downstream of the honeycomb, with the primary function of breaking up large-scale eddies and enhancing small-scale homogenization prior to the contraction, in accordance with established wind-tunnel design practices [39]. The selected geometrical parameters for both the honeycomb and the turbulence screen are consistent with commonly adopted ranges for low-turbulence wind tunnel settling chambers and are based on the design criteria reported by Barlow et al. [5] Chap. 3.4, allowing these components to operate in tandem to minimize flow non-uniformities and reduce turbulence intensity before the air enters the contraction nozzle, while maintaining structural robustness and low pressure losses. In particular, the screen is secured within a dedicated frame composed of fixed and movable sections. Bolted joints connect these sections, enabling precise adjustment of both the mesh positioning and the applied screen tension. All ducts of the wind-tunnel circuit are accessible through dedicated inspection windows, allowing maintenance and specific cleaning operations of the screen and honeycomb when required.

2.3. Collector

Differently from conventional closed-circuit wind tunnels, no diffuser is installed downstream of the test section. Instead, the free jet develops within the anechoic chamber and is subsequently captured by the collector. Therefore, consistently with design practices for open-jet aeroacoustic wind tunnels [19], the collector inlet does not operate as a classical diffuser but rather as a jet-capturing device, and its sizing was defined accordingly. The cross-sectional dimensioning of the collector inlet is a key design concern in open-jet aeroacoustic wind tunnels [12] and is primarily driven by the need to safely ingest the expanding free jet, thereby avoiding flow spillage into the anechoic chamber [40]. Flow spillage is a primary driver of low-frequency jet pulsations that can contaminate and increase background noise measurements [41]. In addition, a sufficiently large capture area is also required to accommodate jet spreading and entrainment of surrounding quiescent air before entering the duct. Moreover, a generous ratio between collector and nozzle exit area is useful to accommodate the downwash and jet deflection induced when testing high-lift aerodynamic models at high angles of attack.

In this configuration, the collector inlet area was selected to be 6.4 times larger than the nozzle exit area. To contextualize this choice within established aeroacoustic wind tunnel design practices, Table 3 compares the geometric and operational parameters of sample prominent aeroacoustic open-jet wind tunnels, where collector dimensions are available from literature.

The comparative geometric metrics show that collector-to-nozzle area ratio (A_{coll}/A) varies significantly across institutions, reflecting different engineering trade-offs between pressure recovery, space availability, and jet stability. While large-scale facilities such as ISAE-SUPAERO [32] and Florida State [31] operate with tight, aerodynamically optimized area ratios close to unity, more compact or multi-purpose facilities tend to employ more generous configurations. In this framework, the configuration adopted for the present facility features a robust area ratio representing an optimal design compromise for small-to-medium scale wind tunnels. This relatively large ratio allows for the prevention of flow spillage into the anechoic plenum while mitigating flow-induced noise and maintaining a compact footprint within the laboratory walls.

2.4. Silencers

Silencers were incorporated into the inlet and collector ducts to limit sound levels while producing minimal self-noise resulting from flow interactions. These components were designed and positioned following the classical guidelines for low-speed aeroacoustic wind tunnels [5], mirroring similar layouts and placement criteria successfully adopted in reference aeroacoustic facilities [3,19]. Splitters were designed with a constant section covering the entire height of the ducts. Drawings of both silencer layouts are presented in Fig. 8. The inlet duct silencer is 2.25 m long to provide a settling area before the first corner, thereby reducing incoming turbulence intensity and noise. The collector silencer layout follows a similar design but is 3 m long. Each silencer consists of four modules, i.e., two 100 mm thick elements on the side walls and two 250 mm thick central splitters. The splitters utilize a circular-arc leading edge (125 mm radius), while the trailing edge features a 15° ramp to minimize wake thickness. The modules were constructed from a metallic structure made of 2 mm galvanized perforated steel sheets with 54% open area filled with the same acoustic stone wool elements used for the duct walls' acoustic treatment described previously arranged in multi-layer configuration (see hex pattern in Fig. 8).

2.5. Corners and turning vanes

The present facility includes three corners equipped with turning-vane cascades, i.e., one located upstream of the nozzle and two downstream of the collector. As shown in Fig. 9, the two consecutive modular corners located downstream of the silenced collector adopt a particular layout that allows the heavy drive motor of the facility to be installed at ground level. In addition to the structural and maintenance advantages associated with this solution, specifically the enhanced accessibility related to the duct's modularity and simplified maintenance enabled by the ground-level fan system, the resulting duct arrangement increases the extent of the acoustically treated surfaces, thus contributing to the reduction of acoustic reflections within the circuit.

The geometry of the turning vanes, shown in Fig. 10(a), exploits a circular arc with a turning radius of 200 mm followed by a straight section. This simplified shape was selected among the classical configurations suggested in Barlow et al. [5]. A gap-to-chord ratio of 0.31 was selected in the design of the first corner, thus equipped with 15 turning vanes, in accordance with established guidelines in literature [42], to mitigate flow recirculation on the pressure side of the turning vanes. As concerns the other two corners, geometrically identical turning vanes were arranged while maintaining the same gap considered for the first corner (i.e., 104 mm), thus increasing their number to 19 due to the larger duct dimensions. This non-insulated, thin-sheet geometry provides an optimal trade-off between aerodynamic turning efficiency and pressure loss

Table 3
Geometric scaling metrics of collector inlet area with respect to nozzle exit area in state-of-the-art aeroacoustic wind tunnels.

Wind Tunnel Facility	Nozzle Dim. $w \times h$ [m]	Nozzle Area $A = w \times h$ [m^2]	Collector Dim. $W_{coll} \times H_{coll}$ [m]	Collector Area $A_{coll} = W_{coll} \times H_{coll}$ [m^2]	Area Ratio A_{coll}/A
Bristol [19]	0.5×0.775	0.3875	2.3×1.9	4.37	11.3
Cottbus [20]	⌀ 0.35	0.0962	0.8×0.8	0.64	6.65
Penn State [28]	0.6×0.6	0.36	1.22×0.91	1.11	3.08
AWB-DLR [29]	0.8×1.2	0.96	1.96×1.96	3.84	4
Univ. of Florida [22]	1.12×0.74	0.83	1.21×0.798	0.965	1.16
Florida State [31]	1.219×0.94	1.145	1.6×1.3	2.08	1.8
ISAE-SUPAERO [32]	1.8×1.8	3.24	2.1×2.1	4.41	1.36
Politecnico di Milano	0.5×0.7	0.35	1.5×1.5	2.25	**6.4**

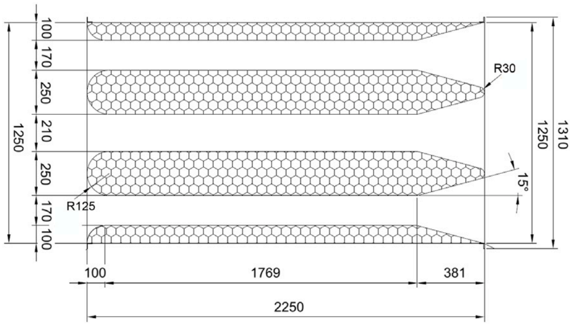

(a) Inlet duct silencer

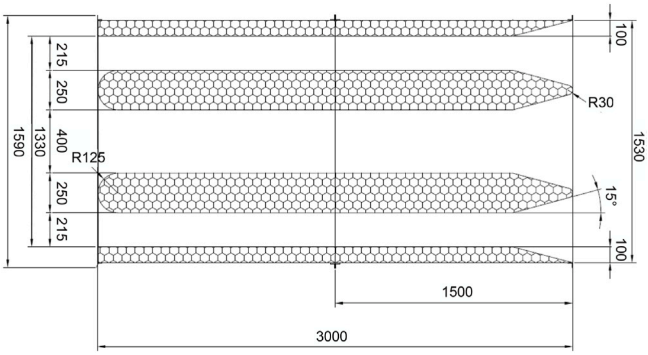

(b) Collector duct silencer

Fig. 8. Drawings of the silencers included in the inlet and collector duct of the anechoic wind tunnel (dimensions in mm, hex pattern indicates the presence of insulating material).

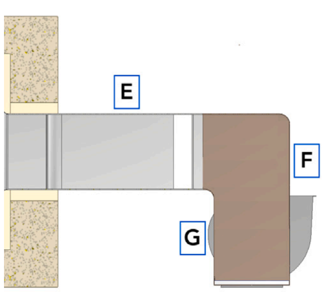

(a) Front view

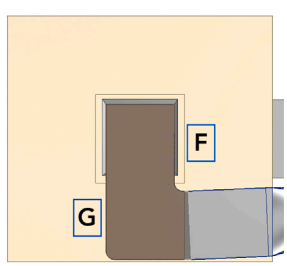

(b) Lateral view

Fig. 9. Details of the second and third corners (F and G) with turning vanes.

reduction, while ensuring manufacturing simplicity. Moreover, the subsequent acoustic qualification of the facility confirmed that the absence of internal sound-absorbing insulation within the vanes did not compromise the acoustic targets of the project, proving that filled turning vanes could not be considered as a critical requirement for a facility of this scale.

2.6. Centrifugal fan

Following standard guidelines for wind tunnel design, the fan was installed at the end of the wind tunnel open-circuit to work in a suction configuration. A centrifugal fan was selected for the present design due to its ability to achieve a high-pressure gain within a compact volume. Indeed, the fan selection process is among the most critical challenges in anechoic wind tunnel design, as it can be considered the component introducing the highest level of noise. As a matter of fact, the more the

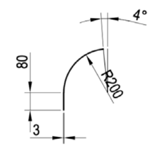

(a) Turning vane geometry

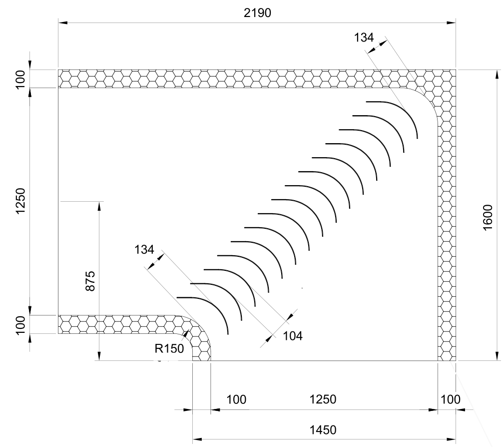

(b) Turning vanes arrangement in the first corner

Fig. 10. Detail of the first corner and turning vanes design choice (dimensions in mm, hex pattern indicates the presence of insulation material).

Table 4
Pressure losses analysis along the wind tunnel components at the design velocity condition $V_\infty = 30$ m/s.

	Δp [Pa]	K_i [-]	% Δp_{total}
Silenced Inlet duct (A)	16.26	0.0295	3.47
First Corner (B)	2.44	0.0044	0.52
Settling Chamber (Honeycomb + Turbulence Screen)	47.11	0.0855	10.05
Contraction Nozzle (C + straight extension)	37.97	0.0688	8.09
Open Test Section - Jet (D)	171.96	0.3119	36.68
Silenced collector (E)	142.28	0.2581	30.35
Second + Third Corners (F + G)	44.01	0.0798	9.39
Rectangular-to-round section (H + Straight duct)	6.77	0.0122	1.45
Total	468.8	0.85	100

sound pressure level produced by the fan is minimized, the more the costs related to duct system sound insulation can be reduced. Typically, in anechoic wind tunnels, fans operate at low angular velocity to reduce the tonal noise at the blade passing frequency and in a working regime near maximum efficiency. The centrifugal fan was sized considering the operating freestream velocity of 30 m/s, requiring a volumetric flow rate of 10.5 m^3/s. In order to evaluate power requirement for the driving fan, the total pressure losses along all the components of the wind tunnel circuit at the design condition, i.e., $V_\infty = 30$ m/s at the nozzle exit, were evaluated on the basis of the established methods reported in Barlow et al. [5]. Table 4 reports the pressure drops calculated for each component (Δp_i), as well as the non-dimensional pressure loss coefficients (K_i) normalized with respect to the design velocity condition at the nozzle exit ($\Delta p_i / 0.5 \rho V_\infty^2$).

Pressure drop analysis highlights that the overall pressure drop is strongly dominated by the downstream components, namely the test section and the silenced collector, which together account for more than 67% of the total losses. In contrast, the flow conditioning elements (i.e., honeycomb, turbulence screen, and inlet region) contribute approximately 14% of the total pressure drop, confirming that their design provides effective turbulence management with a limited energetic penalty. To account for these calculated nominal losses (i.e., 468.8 Pa), the fan system has been sized based on a required overall static pressure rise of 500 Pa, ensuring a sufficient operating margin to accommodate minor modeling uncertainties and off-design variations.

Therefore, similarly to what has been done at the University of Bristol facility, a Ferrari FR 1121 N centrifugal fan [5]) was selected to drive air in the wind tunnel, characterized by a 37 kW maximum installed power and with an electrical power consumption of 10 kW experimentally measured at the target operating conditions ($V_\infty = 30$ m/s). As a result of adopting proper design margins particularly for the fan selection, the wind tunnel is capable of reaching a maximum velocity of approximately 42 m/s, representing the upper operational speed limit of the facility. The fan is placed in a room adjacent to the wind tunnel circuit (see Fig. 1), separated by a thick concrete wall at a distance of about 8 m from the anechoic chamber. The fan unit is mounted on vibration-isolated supports to reduce the transmission of structural vibrations to the ground and the wind tunnel structure. In addition, the connection between the fan and the wind tunnel circuit is implemented through flexible elements (bellows), providing mechanical decoupling and reducing the transmission of vibrations from the rotating machinery to the facility.

3. Wind tunnel qualification

3.1. Aerodynamic qualification

In accordance with the procedures followed in studies of similar open-jet facilities [19,20], an aerodynamic characterization of the jet inside the test chamber was performed prior to investigating the acoustic performance, as is standard practice for conventional wind tunnels. This activity was aimed at ensuring flow quality, particularly by investigating parameters such as velocity uniformity and turbulence intensity across several planes downstream of the nozzle outlet section. To this end, a dual-axis traversing system covering a transversal area downstream of the nozzle outlet (see Fig. 11) was used for velocity and turbulence surveys along the jet for several freestream velocities within the wind tunnel's operational range. Flow surveys were performed using a custom LabVIEW routine, which enabled the control of probe positioning and data acquisition.

Flow uniformity surveys were performed using an elliptical Pitot tube mounted on a supporting strut attached to the vertical guide of the traversing system (see Fig. 11). The pressure signals were acquired using DRUCK LPM Series differential pressure sensors with full-scale (F.S.) ranges of 100 Pa and 2000 Pa (depending on the velocity measurement conditions) and an accuracy of $\pm 0.5\%$ F.S. Data acquisition was performed using a National Instruments NI-9215 module with a sampling frequency of 1 kHz. A finer rectangular map (Map A) was covered by the probe at a freestream velocity $V_\infty = 30\,\mathrm{m/s}$, representing, as previously stated, a representative cruise velocity for typical AAM case studies to be conducted in the facility. In addition, a cross-shaped map (Map B) was considered for the characterization of flow uniformity within the freestream velocity range of the facility, i.e., $10\,\mathrm{m/s} < V_\infty < 40\,\mathrm{m/s}$ with a step of $10\,\mathrm{m/s}$. Fig. 12(a) and (b) show, respectively, the finer and coarser grids of the measurement points, as well as their location with respect to the reference system $X - Y - Z$ used for the qualification activity. The acquisition time for each Pitot measurement point was set to 5 s, and results were averaged to obtain the velocity distributions over the investigated areas.

Turbulence intensity surveys were performed using a hot-wire anemometry system. In particular, a Dantec StreamLine constant temperature anemometer (CTA) and a single-wire probe (type 55P11) were used. The hot-wire probe was mounted on the same automated traversing system employed for the Pitot probe, allowing for an *in-situ* calibration directly inside the wind tunnel test section. During the calibration procedure, the two instruments were positioned side-by-side in the potential core of the jet to ensure they experienced the identical nominal freestream velocity (V_∞). The hot-wire calibration was performed

[5] https://www.ferrariventilatoren.de/wp-content/uploads/2023/02/1-FR.pdf.

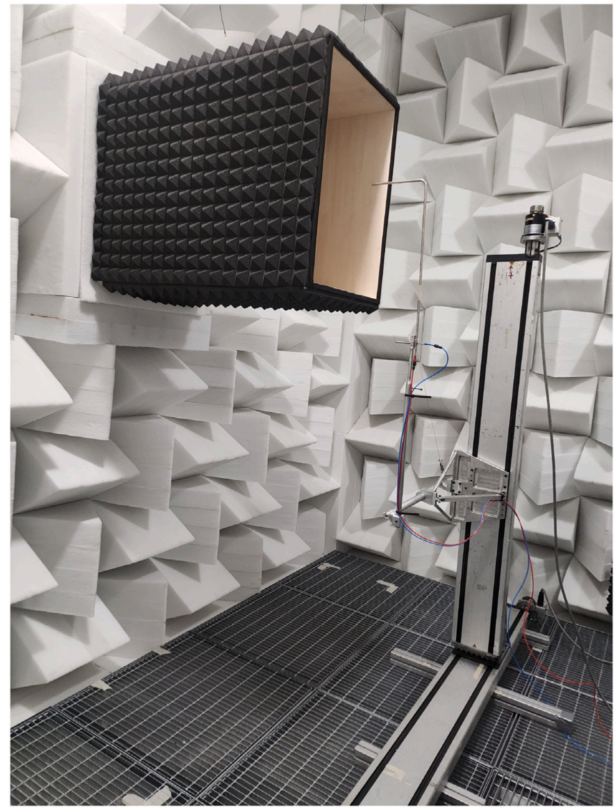

Fig. 11. Probe traversing system used for the jet aerodynamic qualification inside the anechoic test chamber.

by correlating the probe voltage response to the wire-based Reynolds number ($Re_{hw} = \rho V_\infty d_{hw}/\mu$). This approach explicitly accounts for both velocity and ambient temperature variations during the test campaigns, as temperature-induced changes in fluid density and dynamic viscosity are intrinsically compensated within the Reynolds number formulation. The calibration curve was obtained by fitting the experimental data with a 4th-order polynomial, which is a common practice in hot-wire anemometry when extending the classical King's law formulation [43,44].

Mean velocity measurements performed with the present single hot-wire anemometer system show an experimental uncertainty of approximately $\pm 2\%$ evaluated by comparison with Pitot tube measurements, in accordance with the manufacturer's specifications and the established calibration procedures used in the present activity [45]. The turbulence characterization was conducted by again combining a rectangular and a cross-shaped map. Nevertheless, the rectangular map (Map C) used for hot-wire measurements (see Fig. 12(c)) was defined to be equally spaced and coarser than the one used for the Pitot measurements. An acquisition time of 10 s with a sampling frequency of 25 kHz was used for each hot-wire measurement point with no analog filtering. Measurements with the Pitot and hot-wire probes were repeated at five longitudinal distances with respect to the nozzle outlet plane, expressed as fractions of its hydraulic diameter (D_h), i.e., from $X/D_h = 0.11$ to $X/D_h = 1.7$.

Fig. 13 shows a comparison of the axial velocity component V profiles measured at two representative freestream velocities for the facility use, i.e., $V_\infty = 30$ m/s and $V_\infty = 40$ m/s, along the Y- and Z-axes (Map B) at different longitudinal distances (X/D_h). Non-dimensional velocity profiles normalized with respect to the freestream velocity V_∞ are plotted with respect to non-dimensional Y/w and Z/h coordinates, where w and h are, respectively, the length and height of the nozzle outlet section, to highlight the area of the jet exhibiting uniform flow characteristics. The averaged velocity profiles exhibit a top-hat distribution,

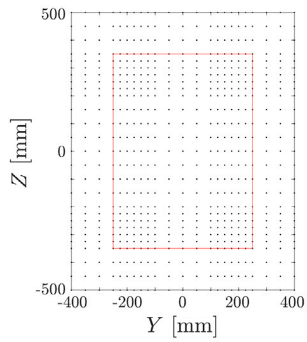

(a) Rectangular map employed for Pitot probe measurements (Map A)

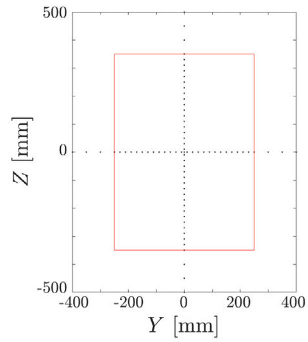

(b) Cross-shaped map employed for Pitot and hot-wire probe measurements (Map B)

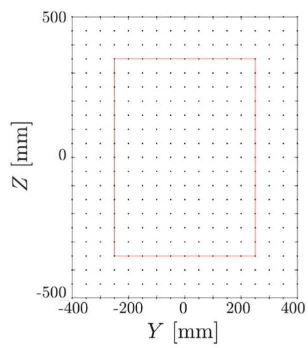

(c) Rectangular map employed for hot-wire probe measurements (Map C)

Fig. 12. Map schemes utilized for the aerodynamic qualification of the jet flow by the two-dimensional traversing system; the red line outlines the nozzle outlet section.

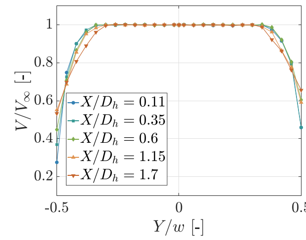

(a) Velocity profile along Y, $V_\infty = 30$ m/s.

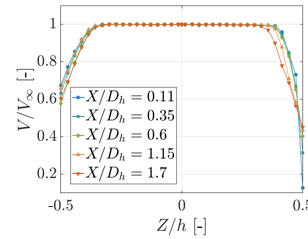

(b) Velocity profile along Z , $V_\infty = 30$ m/s.

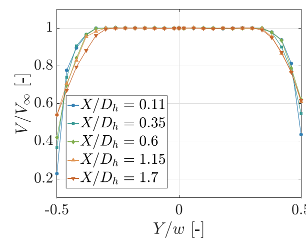

(c) Velocity profile along Y , $V_\infty = 40$ m/s.

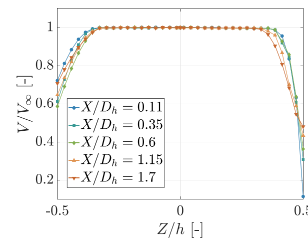

(d) Velocity profile along Z , $V_\infty = 40$ m/s.

Fig. 13. Comparison of the non-dimensional axial velocity profiles measured along the Y and Z directions at different longitudinal distances X/D_h and two wind tunnel freestream velocities.

particularly near the nozzle outlet section, which gradually assumes a Gaussian shape with increasing longitudinal distances, revealing, as expected, the development of the jet shear layer. Moreover, the velocity profiles show a quite similar behavior across the horizontal and vertical extents at the different streamwise distances considered, thus indicating a quite good uniformity of the flow along the jet. A quantitative evaluation of the flow uniformity is calculated as the difference between the maximum and minimum velocity measured inside the constant area of the horizontal and vertical profiles (jet potential core) and expressed as a percentage of V_∞ to be compared with values provided by other similar facilities, reported in Tab. 5. Indeed, in the present facility flow uniformity was found to be approximately 1.4% at target velocity of 30 m/s, thus comparable with the values declared by state-of-the-art aeroacoustic wind tunnels considered as reference.

Flow uniformity evaluation is further supported by the non-dimensional axial velocity contours plotted on the rectangular map (Map A) at the different considered longitudinal distances X/D_h for V_∞ = 30 m/s, as shown in Fig. 14. This representation of the results enables the identification of the jet effective section, characterized by a uniform flow, to be considered for the tests with the model positioned at different planes downstream of the nozzle outlet section. In particular, this effective jet area slightly decreases in size toward the central transverse plane of the anechoic chamber due to the development of the shear layer of the free jet.

The turbulence intensity (TI) was computed from the hot-wire measurements as follows,

$$TI = \sigma_v / V_\infty \cdot 100\ \%, \quad (3)$$

where σ_v is the standard deviation of the instantaneous streamwise velocity component, representing its root-mean-square (RMS) fluctuation about the mean value. A 4th-order Butterworth band-pass filter was applied to the hot-wire signals, with a high-pass cutoff at 4 Hz to remove low-frequency drift and a low-pass cutoff at 10 kHz to attenuate high-frequency electronic noise. The same signal processing chain was applied consistently to all measurement points and planes. Fig. 15 shows the comparison of the turbulence intensity (TI) profiles at different longitudinal distances from the nozzle outlet, again evaluated at V_∞ = 30 m/s and V_∞ = 40 m/s. Turbulence intensity contour plots on the rectangular Map C are also shown in Fig. 16 for measurements performed at V_∞ = 30 m/s.

Table 5
Main jet characteristics in state-of-the-art aeroacoustic wind tunnels, reference freestream velocity in brackets.

Wind Tunnel Facility	TI [%] (V_∞ [m/s])	Flow uniformity [%] (V_∞ [m/s])
Bristol [19]	0.12 (30)	N/A
Cottbus [20]	< 0.2 (20 - 70)	2 (N/A)
Penn State [28]	0.05 (22)	N/A
AWB-DLR [29]	0.3 (60)	N/A
Univ. of Florida [22]	0.11 (17)	2.5 (17)
Florida State [31]	0.07 (15)	1 (N/A)
Southampton [3]	0.1 (60)	4.6 (N/A)
Adelaide [30]	≈ 0.4 (30)	0.3 (20)
DTU (Paul la Cour) [33]	< 0.1 (N/A)	N/A
LANT [10]	0.057 (25)	1 (15)
Politecnico di Milano	0.14 (30)	1.4 (30)

The hot-wire anemometry results confirm the remarkable quality of the flow, particularly showing a quite uniform turbulence intensity level below 0.2% in the core of the profiles downstream of the nozzle outlet section for $X/D_h \leq 0.6$. As can be expected due to the free jet development, the turbulence intensity level slightly increases while moving away from the nozzle outlet, reaching a value of about 1% toward the anechoic chamber's central plane at $X/D_h = 1.7$. A specific set of single-point measurements was conducted by placing the hot-wire probe at the centerline of the jet across different streamwise sections. For these runs, the sampling frequency was kept at 25 kHz, while the acquisition time was increased up to 100 s to evaluate turbulence levels and spectra. This extended duration was adopted selectively, as the longer recording times required were not considered feasible for the extensive

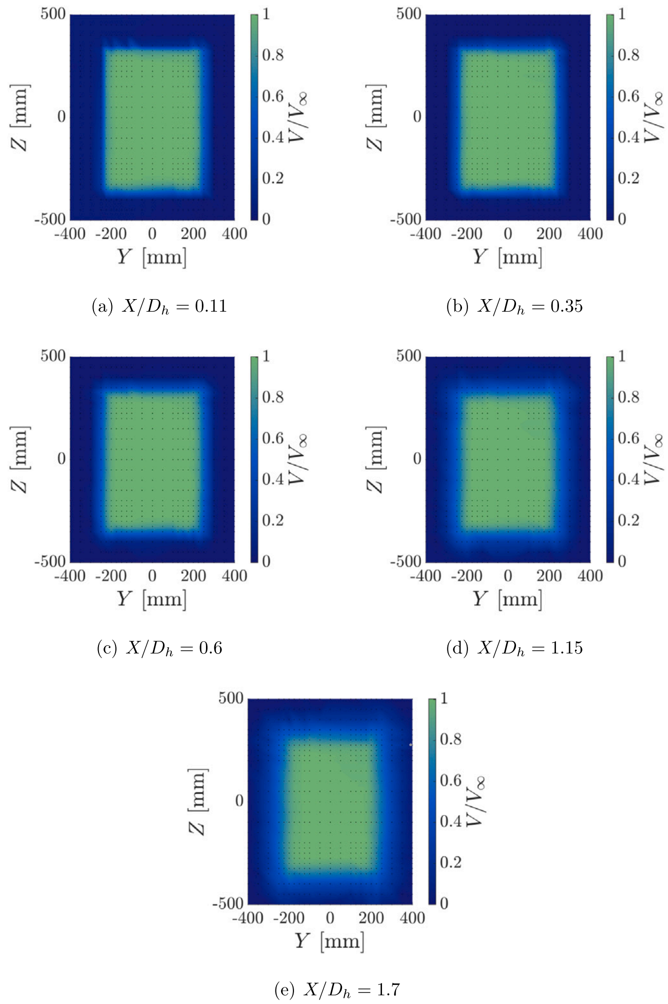

(a) $X/D_h = 0.11$ (b) $X/D_h = 0.35$ (c) $X/D_h = 0.6$ (d) $X/D_h = 1.15$ (e) $X/D_h = 1.7$

Fig. 14. Comparison of the non-dimensional axial velocity contours measured on the rectangular map a at different longitudinal distances X/D_h and $V_\infty = 30$ m/s.

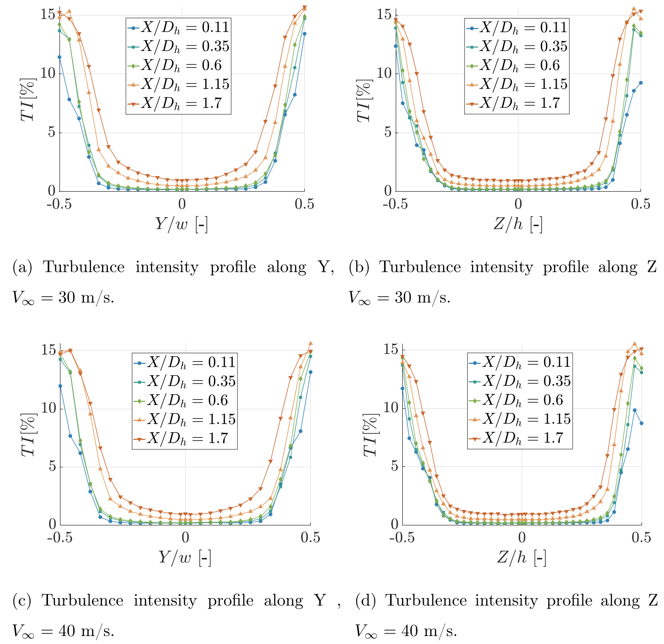

(a) Turbulence intensity profile along Y, $V_\infty = 30$ m/s. (b) Turbulence intensity profile along Z, $V_\infty = 30$ m/s. (c) Turbulence intensity profile along Y, $V_\infty = 40$ m/s. (d) Turbulence intensity profile along Z, $V_\infty = 40$ m/s.

Fig. 15. Comparison of the turbulence intensity profiles measured along the Y and Z directions at different longitudinal distances X/D_h and two wind tunnel freestream velocities.

profile and mapping surveys. However, this choice enabled successfully improving the convergence of the low-frequency content and reducing the statistical uncertainty of both the turbulence intensity and velocity spectra.

A quantitative comparison of turbulence intensity values provided by prominent aeroacoustic wind tunnels is reported in Tab. 5. The turbulence intensity level measured for the present facility is found to be equal to 0.14% just behind the nozzle outlet section, i.e., $X/D_h = 0.11$. In particular, this value is well within the range of values measured in state-of-the-art aeroacoustic facilities considered as reference, where turbulence intensity levels measured near the nozzle outlet are between 0.05% and 0.3%.

For completeness, the turbulent velocity fluctuations were analyzed in the frequency domain by computing the one-dimensional power spectral density of the streamwise velocity component, ($S_{uu}(f)$) to show the energy content of eddies of a certain size. Fig. 17 shows the comparison of the spectra obtained from hot-wire measurements at the jet centerline point for different streamwise distances from the nozzle outlet, at freestream velocity of 30 m/s and for different velocities at fixed distance $X/D_h = 0.6$, with the increased acquisition time of 100 s. The turbulence spectra were computed using Welch's method, with the 25 kHz sampled signals filtered as previously described. The power spectral density was estimated by dividing the signal into Hamming-windowed segments of 4096 samples, with 50% overlap between consecutive segments, while an FFT length of 2^{14} points was used for the computation of each modified periodogram. The final spectrum was obtained by averaging all modified periodograms.

The observed broadband character of the turbulence spectra without tonal peaks confirms the absence of periodic vortex shedding. Moving along the frequency axis, the shift toward lower-frequency dominance of the bump shown in Fig. 17(a) is consistent with the increasing scale of the turbulence downstream from nozzle exit. Specifically, this broadband hump observed in the range between 20 and 30 Hz represents the energetic signature of the large-scale coherent vortical structures originating within the jet's shear layer. By scaling this frequency range with the nozzle hydraulic diameter (D_h) and the nominal freestream velocity ($V_\infty = 30$ m/s), the resulting Strouhal number aligns with the typical jet-instability and vortex-merging frequencies documented in open-jet literature [46]. As these shear-layer instabilities advect downstream, they undergo a natural growth and pairing process, which also explains the energy shift toward lower frequencies along the centerline [47]. This scaling behavior is further confirmed by evaluating the spectra at a fixed spatial location ($X/D_h = 0.6$) across different flow velocities, as shown in Fig. 17(b). When plotted against the Strouhal number, the energetic humps remain strictly aligned at the same St position, while the curves scale upward with increasing velocity. This upward shift reflects the expected increase in turbulent kinetic energy injected into the system, while the invariant Strouhal position confirms that the characteristic frequency of these coherent structures scales linearly with freestream velocity. Moreover, in the frequency range between 300 and 1000 Hz, the spectra exhibit a slope approximately consistent with the $-5/3$ scaling associated with the onset of the inertial subrange of turbulence [44], as graphically shown in Fig. 17(a).

Hot-wire measurements across the cross-sectional grid at the different downstream locations also allowed the estimation of the shear layer thickness from the spatial distribution of the mean streamwise velocity profiles. The shear layer thickness δ is calculated by using 6 times the corresponding momentum thickness [48] calculated according to Göertler's theory [49]. Fig. 18 shows the estimated growth of the shear layer thickness along the streamwise direction (X axis) referred to both

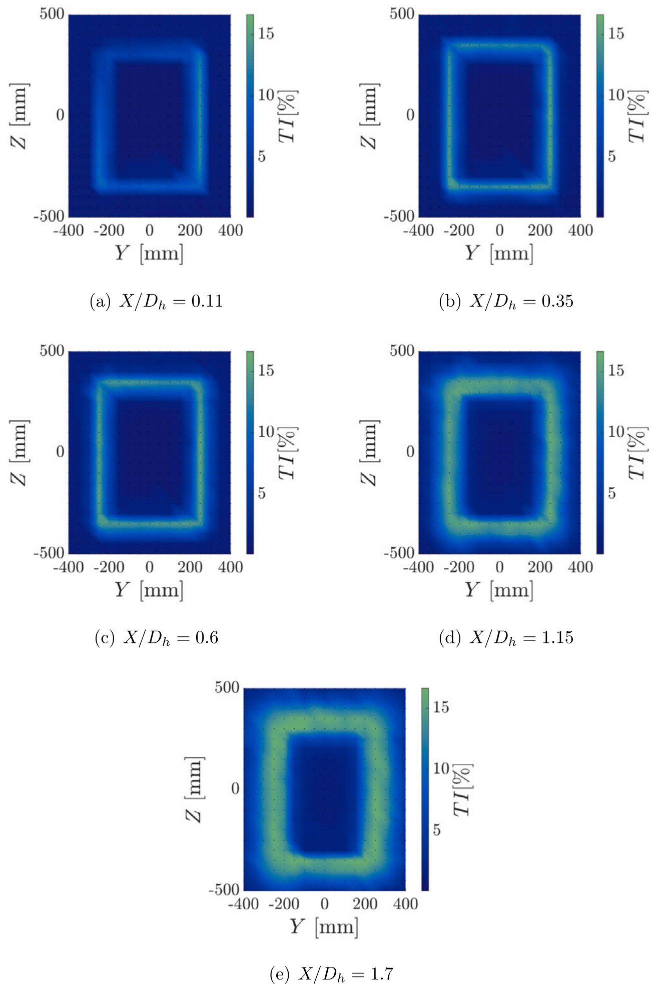

Fig. 16. Comparison of the turbulence intensity contours measured on the rectangular map C at different longitudinal distances X/D_h and V_∞ = 30 m/s.

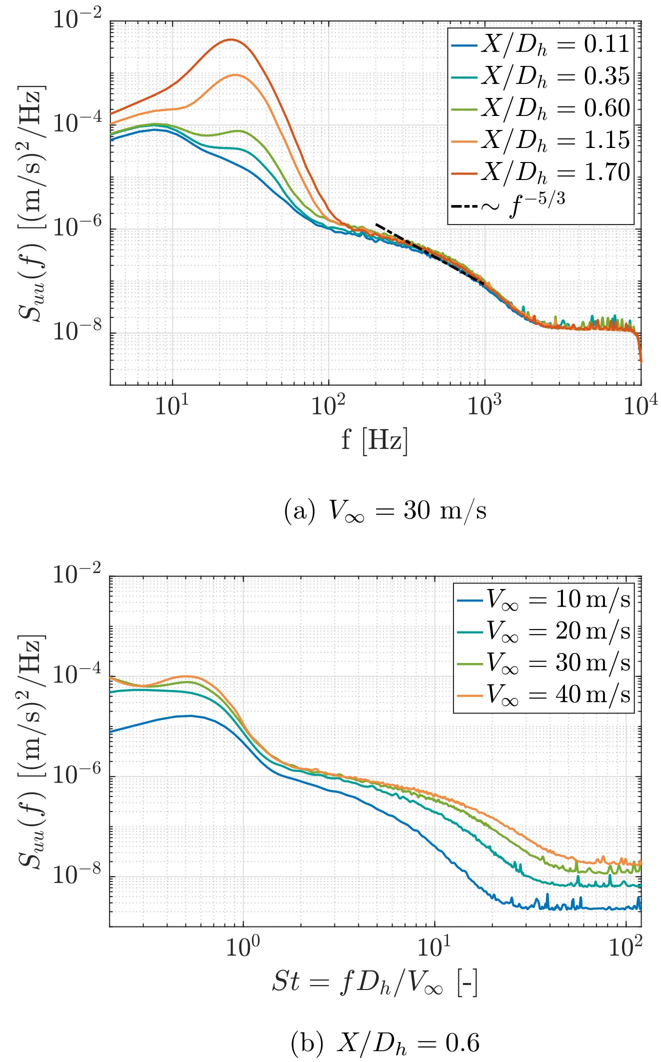

Fig. 17. One-dimensional power spectral density of the streamwise velocity component spectrum.

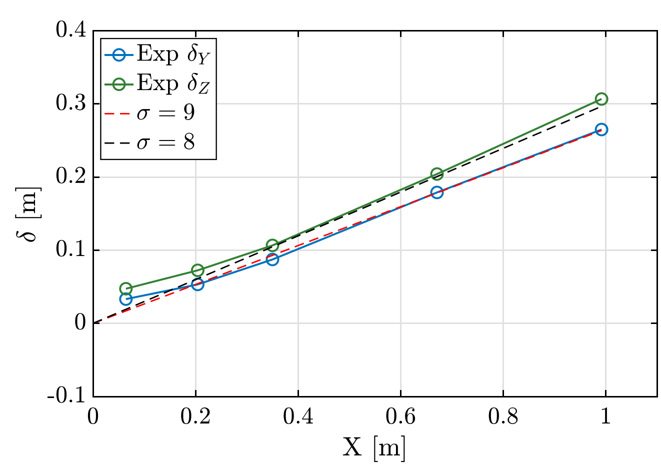

Fig. 18. Shear layer thickness growth along the streamwise direction, evaluated for both the Y and Z directions at 30 m/s, compared to Göertler's theory [49] with σ = 8 and σ = 9.

the horizontal and vertical velocity profiles, i.e., δ_Y and δ_Z respectively, measured at 30 m/s. In accordance with what was found by similar experimental studies conducted in the open-jet Small Anechoic Wind Tunnel (KAT) of the National Aerospace Laboratory (NLR) and the DNW-PLST wind tunnel [50], the shear layer grows linearly with downstream distance except for a small deviation observed at the nearest point to nozzle outlet section. In particular, the present measured trend shows a good agreement with the theoretical shear layer thickness evaluated with the linear analytic law retrieved by Göertler [49],

$$\delta(X) = \frac{6X}{\sigma\sqrt{2\pi}} \tag{4}$$

where the parameter σ is defined as spreading rate. In particular, experimental data retrieved from the hot wire measurements show a good agreement with the theoretical shear layer thickness for a spreading rate of $\sigma = 9$ and $\sigma = 8$, comparable to the value reported for the shear layer characterization in the similar open-jet Small Anechoic Wind Tunnel (KAT) of the National Aerospace Laboratory (NLR) [50].

3.2. Acoustic qualification

In addition to aerodynamic performance criteria, namely high flow uniformity and low turbulence intensity along the jet, aeroacoustic wind tunnels must guarantee a low background noise level as well as near-anechoic conditions for highly accurate noise measurements [19]. To verify these acoustic requirements, a dedicated measurement campaign was performed to estimate the jet flow background noise of the new POLIMI-DAER facility and compare it with the performance of existing facilities. In addition, the capability of the anechoic wind tunnel to perform far-field noise measurements was evaluated through two additional campaigns focused on the noise generated by simple-shaped bodies immersed in the flow, i.e., a circular cylinder and an airfoil. All the acoustic measurements performed during this qualification activity employed a GRAS 40PL-10 CCP microphone mounted on a movable support, allowing for changes in the orientation of the microphone diaphragm and the location of the measurement point along the test chamber centerline under the jet. The microphone was equipped with a standard spherical foam wind-screen to reduce flow-induced noise. The use of a nose cone was not considered, as the microphone was not directly exposed to the flow. For the present measurements the signal was acquired for a duration of 20 s at a sampling rate of 25.6 kHz. Results in this section are reported as the power spectral density of the noise spectra, calculated using Welch's method. The segment length was defined based on the target frequency resolution $\Delta f = 8$ Hz as $n_{perseg} = f_s/\Delta f$. A Hann window was applied to each segment, with 50% overlap between adjacent segments. The spectra were obtained by averaging the periodograms of the windowed segments, resulting in power spectral density estimates expressed in Pa^2/Hz. All spectra are referenced to the reference sound pressure of 20×10^{-6} Pa. The time-domain signals were filtered with a band-pass filter to remove components below the facility cut-off frequency (i.e., 150 Hz).

3.2.1. Jet flow background noise

The jet background noise qualification campaign utilized a microphone placed at $(X, Y, Z) = (0\text{ m}, 0\text{ m}, -0.7\text{ m})$, i.e., vertically positioned below the center of the nozzle outlet section, corresponding to a polar angle $\theta = 90°$ relative to the horizontal X-axis. Furthermore, the microphone was repositioned at $(X, Y, Z) = (0.7\text{ m}, 0\text{ m}, -0.7\text{ m})$, oriented to a polar angle $\theta = 45°$, to evaluate the noise directivity of the free jet. Acoustic measurements were performed for freestream wind tunnel velocities ranging from 10 m/s to 40 m/s, in increments of 5 m/s. Fig. 19 presents the narrowband background noise spectra evaluated by the microphone at these increasing velocities for both polar angles, namely $\theta = 45°$ and $\theta = 90°$.

A smooth and gradual decay of the spectral curves is observed for both polar angles, which is consistent with the background noise spectra behavior typically reported in the acoustic qualification of similar facilities [3,19]. In particular, the background noise reaches the noise floor of the anechoic chamber for high frequencies at freestream velocities up to 25 m/s, particularly for the microphone at $\theta = 90°$ and similarly to what is observed at the University of Bristol facility [19]. Moreover, to provide a quantitative comparison with the acoustic performance of similar facilities, the A-weighted overall sound pressure level ($OASPL_A$) measured at various freestream velocities for $\theta = 45°$ and $\theta = 90°$ was evaluated from the previous measurements. In particular, the $OASPL_A$ was scaled accounting for the nozzle outlet area (A) and the different microphone distance from the nozzle outlet center (r), as follows:

$$OASPL_{A_s} = OASPL_A - 10\log_{10}\left(\frac{A}{r^2}\right). \tag{5}$$

The $OASPL_{A_s}$ curves comparison reported in Fig. 20 shows that the background noise levels evaluated for $\theta = 45°$ and $\theta = 90°$ in the POLIMI-DAER wind tunnel are comparable to those of state-of-the art facilities with similar characteristics. In particular, measurements performed at polar angle $\theta = 90°$ exhibit slightly lower $OASPL_{A_s}$ values compared to other facilities, especially from freestream velocities greater than 25 m/s. Moreover, from this velocity onward, $OASPL_{A_s}$ scales linearly with the logarithm of the velocity, consistent with results obtained in other facilities. On the other hand, at lower velocities, the curves exhibit non-linear behavior similar to that found in the University of Bristol wind tunnel. In analogy with the findings of Mayer et al. [19], this could be explained by the narrow spectra of the microphone signals at both polar angles, indicating that below 25 m/s the jet flow background noise reaches the anechoic chamber's noise floor at high frequencies.

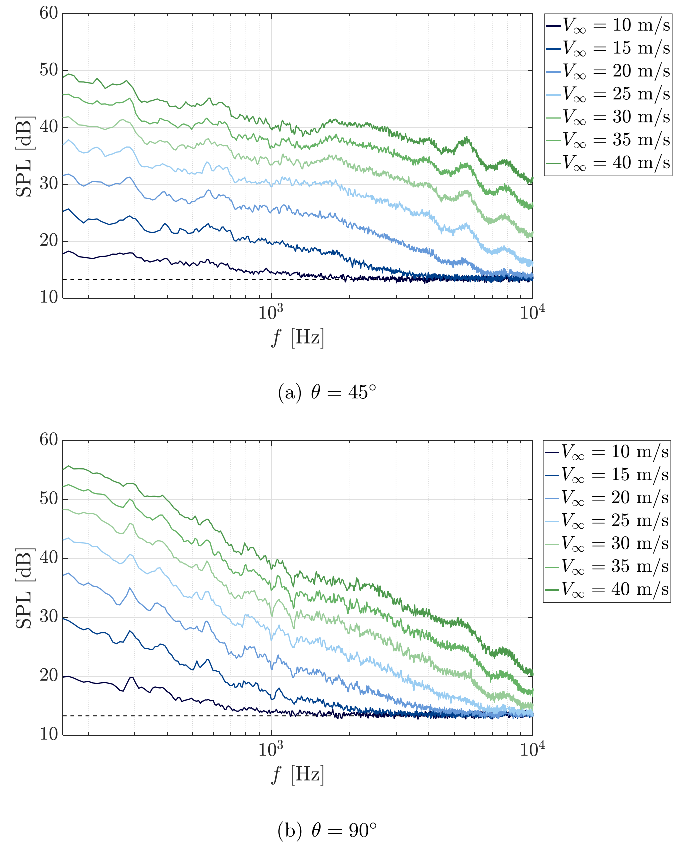

Fig. 19. Comparison of background noise measurements for varying freestream velocity V_∞. The dashed line shows the noise floor of the anechoic chamber measured with the fan turned off.

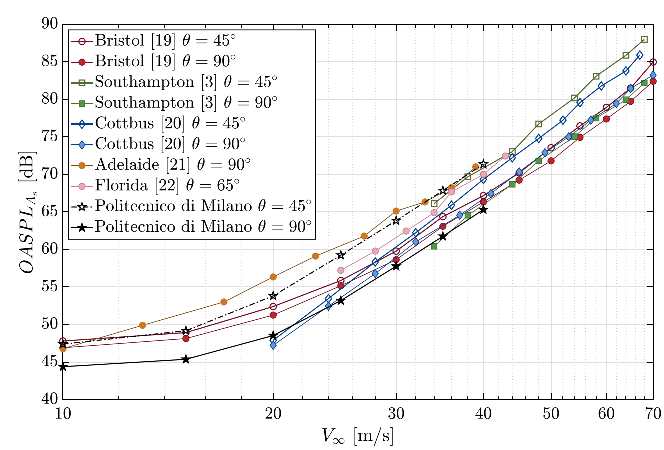

Fig. 20. Comparison of scaled A-weighted OASPL for different aeroacoustic wind tunnel facilities.

For both microphone orientations the velocity scaling of the jet background noise was also investigated through the evaluation of the spectral scaling exponent (N), defined as the logarithmic ratio between the power spectral density at a given velocity (V_1) and the reference spectrum at the maximum velocity of the facility, i.e., $V_2 = 40$ m/s, as follows:

$$N(f) = \frac{\log\left(\frac{PSD_{V_1}(f)}{PSD_{V_2}(f)}\right)}{\log\left(\frac{V_1}{V_2}\right)}, \tag{6}$$

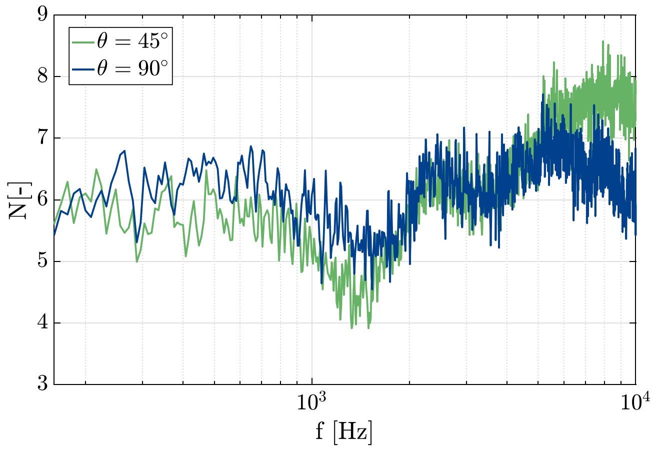

Fig. 21. Background noise velocity scaling for two polar angles.

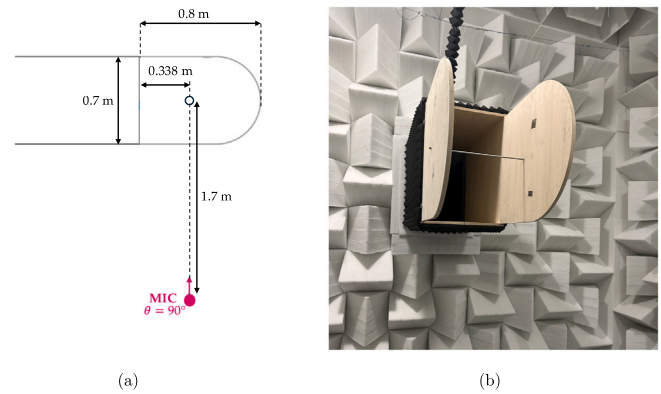

Fig. 22. Experimental setup for the round cylinder far-field noise measurements.

where PSD_V is the power spectral density at the velocity V and V_1 and V_2 are the two velocities considered to calculate $N(f)$. The exponent therefore represents the local velocity scaling of the background noise spectrum, as $PSD_V(f) \propto V^{N(f)}$. In particular, average values of $N(f)$ were obtained for the two microphone polar angles considering as V_1 the freestream velocities where the A-weighted OASPL scales linearly with $log(V)$, i.e., from 25 m/s to 35 m/s.

The behavior of the average scaling factor as a function of frequency is shown in Fig. 21. The analysis of the plot provides insights into the physical contribution of the jet flow to the measured background noise. In the frequency range between 150 Hz and 5 kHz, results show values of N around 6 for both microphone polar angles, consistent with a dominant dipole-type contribution to acoustic noise [51]. This is typically associated with shear- or boundary layer scattering, such as those occurring at the nozzle lip of open-jet wind tunnels [52]. In the high-frequency range between 5 kHz and 10 kHz, a divergence between the two microphone angles is observed. While the $\theta = 90°$ curve maintains a stable trend around $N \approx 6$, confirming that the dipole-type nozzle lip noise remains the primary acoustic source orthogonal to the flow, the scaling factor for the $\theta = 45°$ shifts upward toward $N \approx 8$. This latter behavior indicates the localized emergence of quadrupole-type sources, consistent with free jet mixing noise [53]. Such a trend is a direct consequence of downstream convective directivity, which preferentially channels high-frequency quadrupole acoustic energy into shallower angles relative to the jet axis. These quadrupole mechanisms, while detectable at higher frequencies and specific forward angles, do not alter the overall dominant dipole nature of the noise in the POLIMI-DAER facility, which operates at a significantly lower freestream speed compared to, for instance, the aeroacoustic wind tunnels at the Universities of Bristol and Southampton [3,19].

3.3. Benchmark noise validation cases

As previously mentioned, the acoustic qualification campaign was supplemented by two additional measurement series involving a circular cylinder and an airfoil. These tests served to evaluate the facility's capability to conduct far-field noise investigations on both bluff and streamlined aerodynamic bodies. The present acoustic results are not corrected for the influence of refraction effects due to shear layer influence [54], as they can be considered negligible for these specific qualification measurements performed at a relatively low Mach number with a far-field microphone at $\theta = 90°$ [55]. Moreover, this choice is coherent with the one used by authors who performed the same benchmark tests for the acoustic qualification of their wind tunnels, not considering such corrections [3,19,20].

3.4. Round cylinder validation case

A first series of far-field noise measurements was conducted using a 0.5 m long steel cylinder with an 8 mm diameter (span-to-diameter ratio of 62.5), used as a benchmark bluff body. The cylinder was mounted at $(X, Y, Z) = (0.338\ \text{m}, 0\ \text{m}, 0\ \text{m})$ between two semicircular wooden end plates with a 0.35 m radius (see dimensions in Fig. 22(a)). Far-field acoustic measurements were collected using a microphone placed at $(X, Y, Z) = (0.338\ \text{m}, 0\ \text{m}, -1.7\ \text{m})$, i.e., 1.7 m below the body and $\theta = 90°$. Fig. 22(b) shows a picture of the cylinder setup inside the anechoic test chamber.

Measurements were performed at three wind tunnel freestream velocities, i.e., 20 m/s, 30 m/s and 40 m/s with and without the cylinder mounted, in order to enable a direct comparison with background noise for each freestream velocity condition. Fig. 23 shows the comparison of the resulting SPL spectra plotted against the Strouhal number calculated considering each freestream velocity and the cylinder diameter (d) as characteristic length. The noise radiated by the cylinder exceeds the jet flow background noise over the entire frequency range. In particular, the SPL values measured with the cylinder in place exceed the background noise by a level in dB comparable to those found in a similar experiment performed at the University of Bristol wind tunnel [19] at the same freestream velocities. The spectra corresponding to the cases with the cylinder present exhibit a pronounced peak at $St \approx 0.2$, corresponding to the Strouhal number governing the vortex shedding from circular cylinders in the range of subcritical Reynolds numbers according to theory of Schlichting and Gersten [56]. Geyer et al. [57] show the link of this major peak with lift force fluctuations. The lower peak around 0.4 appreciable at higher velocities can be related to drag force fluctuations, as also found from the analogous experimental study by Mayer et al. [19]. Globally, these results enable the exploitation of the facility under investigation for the aeroacoustic study of bluff bodies, also engaging more complex geometries, such as fuselages typical of aeronautical model applications.

3.5. Tripped NACA 0012 airfoil validation case

As second benchmark test case, a NACA 0012 airfoil was investigated. An airfoil model with 0.15 m chord (c) was set up between the semicircular end-plates with the leading edge two chords past the nozzle outlet section, as depicted in Fig. 24(a). A metallic cylindrical bar mounted inside the model at 25% of the chord allowed adjustment of the airfoil angle of attack. The microphone was placed at $(X, Y, Z) =$

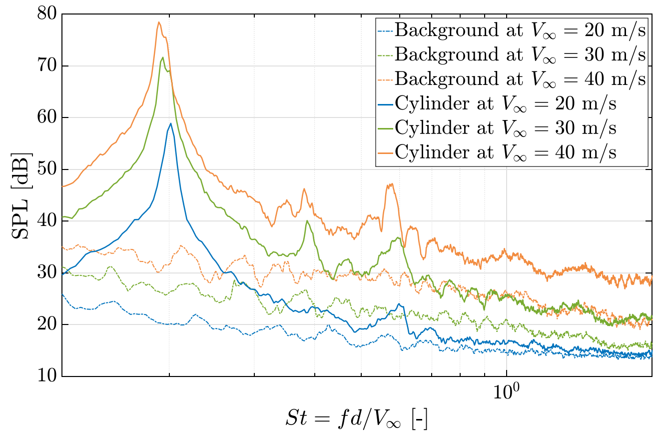

Fig. 23. Far-field noise spectra comparison for cylinder and background noise at different wind tunnel freestream velocities V_∞, $\theta = 90°$.

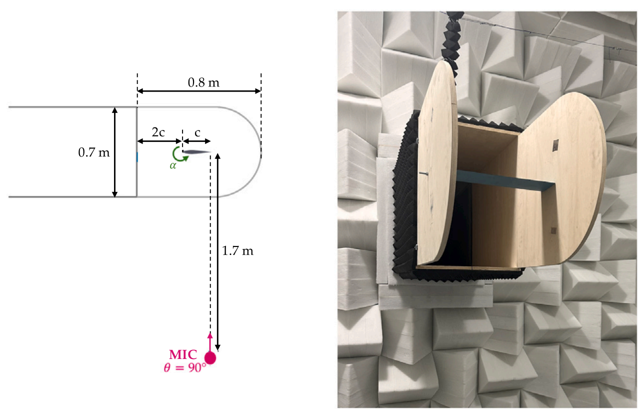

(a) (b)

Fig. 24. Experimental setup for the NACA0012 airfoil far-field noise measurements ($c = 0.15$ m).

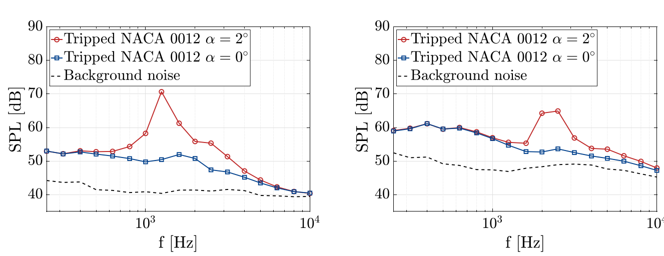

(a) $V_\infty = 30$ m/s (b) $V_\infty = 40$ m/s

Fig. 25. Far-field noise spectra in 1/3 octave bands for the NACA 0012 airfoil with the turbulator tape in comparison with the background noise, $\theta = 90°$.

$(0.45 \text{ m}, 0, -1.7 \text{ m})$, i.e., 1.7 m below the body in correspondence with the airfoil trailing edge and $\theta = 90°$ (see Fig. 24(a)). The airfoil was tripped using a 6 mm wide and 0.5 mm thick zig-zag turbulator trip tape with a turbulator angle of 70° from Glasfaser-Flugzeug-Service GmbH positioned at 10% of the chord, analogously to what has been done by Mayer et al. [19] for similar tests at University of Bristol wind tunnel.

Fig. 25 shows the results at $V_\infty = 30$ m/s and $V_\infty = 40$ m/s for $\alpha = 0°$ and $\alpha = 2°$, compared with the background noise evaluated at the same wind tunnel freestream velocity and the same microphone position. In the range between 150 Hz and 10 kHz, the far-field noise generated by the airfoil is visibly detached from the background noise for both the considered freestream velocities and angles of attack, reaching values above 10 dB up to 3 kHz. A spectral peak can be identified from the airfoil measurements between 1.3 kHz and 3 kHz, showing a tendency to shift slightly toward higher frequencies as the freestream velocity increases and to grow in amplitude while increasing the angle of attack. This is consistent with the fact that for airfoils operating at moderate Reynolds numbers, the acoustic spectrum is known to exhibit a broadband hump associated with the scattering of turbulent boundary layer fluctuations at the trailing edge. The increase in amplitude at a non-zero angle of attack, accompanied by a slight shift of the spectral peak toward lower frequencies, is consistent with established models [58], which predict that the angle of attack primarily affects the turbulence intensity and boundary layer thickness, thereby modifying both the radiated sound levels and the characteristic frequency.

4. Conclusions

The present work has detailed the design, implementation, and comprehensive qualification of a new anechoic wind tunnel facility at the Department of Aerospace Science and Technology of Politecnico di Milano. Developed to address the emerging challenges of Urban Air Mobility and interactional aeroacoustics, the facility represents a strategic asset for the experimental characterization of scaled multi-propeller and distributed electric propulsion systems.

The results of the aerodynamic qualification confirm the high quality of the flow within the test chamber. In the identified potential core the jet exhibits a remarkable degree of uniformity; in particular the mean across the different streamwise sections is 1.4% along both spanwise and vertical directions at $V_\infty = 30$ m/s. Hot-wire anemometry surveys demonstrated a very low turbulence intensity, approximately 0.14% for $V_\infty = 30$ m/s at the minimum distance from the nozzle outlet and maintaining levels below 1% up to the central plane of the anechoic chamber.

From an acoustic perspective, the facility's design—featuring silenced ducts, an optimized centrifugal fan layout, and high-performance anechoic wedges—successfully established a controlled environment with a cut-off frequency of 150 Hz. The acoustic characterization of the background noise floor and the preliminary measurements on benchmark cases (circular cylinder and NACA 0012 airfoil) validated the facility's ability to ensure an adequate detachment of the measured noise signals with respect to jet background noise across its operational range. These parameters meet the stringent requirements for high-fidelity aeroacoustic measurements and are fully consistent with the performance of state-of-the-art academic facilities worldwide.

In conclusion, the newly established facility successfully fills a longstanding infrastructural gap within the Italian academic landscape. Rather than introducing non-standard design features, the wind tunnel relies on validated state-of-the-art design criteria, offering a valuable asset for the scientific advancement of the national aeroacoustics community, particularly for the investigation and development of novel AAM configurations. By successfully balancing high-quality flow uniformity with a controlled acoustic environment, the facility is uniquely positioned to tackle the complexities of next-generation aircraft noise. Future research will prioritize the decoupling of interactional noise sources in multi-rotor configurations, leveraging the integrated microphone arrays to provide high-fidelity data essential for the validation of advanced numerical models and the development of quieter Urban Air Mobility solutions.

CRediT authorship contribution statement

Gemma Bucherelli: Writing – original draft, Visualization, Software, Methodology, Investigation, Data curation, Conceptualization. **Donato Grassi:** Writing – original draft, Supervision, Software, Project administration, Methodology, Investigation, Conceptualization. **Alberto Savino:** Writing – original draft, Supervision, Software, Methodology, Formal analysis, Conceptualization. **Alberto Guardone:** Supervision, Resources, Investigation, Funding acquisition, Conceptualization. **Alex Zanotti:** Writing – review & editing, Writing – original draft, Supervision, Project administration, Methodology, Investigation, Funding acquisition, Data curation, Conceptualization.

Declaration of competing interest

The authors declare that they have no known competing financial interests or personal relationships that could have appeared to influence the work reported in this paper.

Acknowledgements

The work in this study was carried out within the MOST—Sustainable Mobility National Research Center and received funding from the European Union Next-Generation EU (PIANO NAZIONALE DI RIPRESA E RESILIENZA (PNRR) – MISSIONE 4 COMPONENTE 2, INVESTIMENTO 1.4 – D.D. 1033 17/06/2022, CN00000023). This manuscript reflects only the authors' views and opinions, neither the European Union nor the European Commission can be considered responsible for them.

Data availability

Data will be made available on request.

References

[1] Soderman PT, Allen CS. Microphone measurements in and out of airstream. Berlin, Heidelberg: Springer Berlin Heidelberg; 2002. p. 1–61. https://doi.org/10.1007/978-3-662-05058-3_1
[2] Goldstein ME. Aeroacoustics. McGraw-Hill; 1976.
[3] Chong T, Joseph P, Davies P. Design and performance of an open jet wind tunnel for aero-acoustic measurement. Appl Acoust 2009;70(4):605–14. https://doi.org/10.1016/j.apacoust.2008.06.011
[4] Amiet R. Refraction of sound by a shear layer. J Sound Vib 1978;58(4):467–82. https://doi.org/10.1016/0022-460X(78)90353-X
[5] Barlow JB, Rae WH, Pope A. Low-speed wind tunnel testing. Wiley; 1999.
[6] Giardino F. The design, fabrication, and commissioning of a high-speed aeroacoustic wind tunnel for studies of surface pressure fluctuations beneath turbulent boundary layers [Master's thesis]. Department of Mechanical and Aerospace Engineering, Ottawa, Ontario (CA); May 2018.
[7] Brücker C. A low-noise open-jet wind tunnel for aeroacoustic measurements. Exp Fluids 2010;49(5):939–49.
[8] Remillieux M, Crede E, Camargo H, Burdisso R, Devenport W, Rasnick M, Seeters PV, Chou A. Calibration and demonstration of the new Virginia Tech anechoic wind tunnel. In: 14th AIAA/CEAS aeroacoustics conference (29th AIAA aeroacoustics conference); 2008. https://doi.org/10.2514/6.2008-2911
[9] Kröber S. Comparability of microphone array measurements in open and closed wind tunnels [Ph.D. thesis]. Technical University of Berlin; 2013.
[10] Amaral F, Serrano Rico J, Bresci C, Beraldo M, Victorino V, Gennaro E, Medeiros M. The low acoustic noise and turbulence wind tunnel of the university of Sao Paulo. Aeronaut J 2022;126(1297):500–32. https://doi.org/10.1017/aer.2021.80
[11] Soderman PT, Olsen LE. Large-scale aeroacoustic research feasibility and conceptual design of test-section inserts for the Ames 80- by 120-foot wind tunnel. Technical Publication NASA Technical Paper 3020 NASA Ames Research Center: NASA; Dec 1990.
[12] Wiedemann J, Wickern G, Ewald B, Mattern C. Audi AeroAcoustic wind tunnel. SAE Technical Paper 1993. https://doi.org/10.4271/930300 (930300.
[13] Zawodny NS, Haskin RS. Acoustic characterization of a wing-propeller system for distributed electric propulsion aircraft. J Aircr 2021;58(6):1240–56.
[14] Celik A, Syafiqah Jamaluddin N, Baskaran K, Meloni S, Rezgui D, Azarpeyvand M. Experimental characterisation of rotor noise in tandem configuration. Appl Acoust 2024;222:110053. https://doi.org/10.1016/j.apacoust.2024.110053. https://www.sciencedirect.com/science/article/pii/S0003682X24002044.
[15] Granata D, Savino A, Grassi D, Riccobene L, Zanotti A. Aerodynamic and aeroacoustics investigation of tandem propellers in hover for eVTOL configurations. Aerosp Sci Technol 2024;155:109740. https://doi.org/10.1016/j.ast.2024.109740. https://www.sciencedirect.com/science/article/pii/S1270963824008691.
[16] Zanotti A, Granata D, Savino A, Caccia F, Abergo L, Guardone A, Yin J, Wickersheim R, Kessler M, Visingardi A, Barbarino M, Haas A, Kaltenbach H-J, Reboul G, Bernardini G, Poggi C. Acoustic and aerodynamic evaluation of POLIMI tandem propellers in hover and cruise flight conditions within GARTEUR AG26. CEAS Aeronaut J 2025;1869–5590. https://doi.org/10.1007/s13272-025-00903-5
[17] Yin J, De Gregorio F, Rossignol K-S, Rottmann L, Ceglia G, Reboul G, Barakos G, Qiao G, Muth M, Kessler M, Visingardi A, Barbarino M, Petrosino F, Zanotti A, Oberti N, Savino A, Bernardini G, Poggi C, Abergo L, Caccia F, Guardone A, Testa C, Zaghi S. Acoustic and aerodynamic evaluation of DLR small-scale rotor configurations within GARTEUR AG26. CEAS Aeronaut J 2025;16:1175–96. https://doi.org/10.1007/s13272-025-00903-5
[18] Bucherelli G, Das L, Grassi D, Granata D, Zanotti A. Experimental investigation of the acoustic signature of a quad-rotor eVTOL aircraft in hover. In: 51st European rotorcraft forum; 2025.
[19] Mayer Y, Jawahar HK, Szoke M, Ali SS, Azarpeyvand M. Design and performance of an aeroacoustic wind tunnel facility at the university of Bristol. Appl Acoust 2019;155:358–70. https://doi.org/10.1016/j.apacoust.2019.06.005
[20] Sarradj E, Fritzsche C, Geyer TF, Giesler J. Acoustic and aerodynamic design and characterization of a small-scale aeroacoustic wind tunnel. Appl Acoust 2009;70(8):1073–80. https://doi.org/10.1016/j.apacoust.2009.02.009
[21] Leclercq D, Doolan C, Reichl J. Development and validation of a small-scale anechoic wind tunnel. In: Kessissoglou N, editor. Proceedings of the 14th international congress on sound and vibration (ICSV14). Cairns, Australia; 2007, pp. www1–www8, Paper 105.
[22] Mathew J, Bahr C, Carroll B, Sheplak M, Cattafesta L. Design, fabrication, and characterization of an anechoic wind tunnel facility. In: Presented at the 11th AIAA/CEAS aeroacoustics conference (26th AIAA aeroacoustics conference); May 2005.
[23] Zanotti A, Algarotti D. Aerodynamic interaction between tandem overlapping propellers in eVTOL airplane mode flight condition. Aerosp Sci Technol 2022;124. https://doi.org/10.1016/j.ast.2022.107518
[24] Munjal ML. Acoustics of ducts and mufflers. 2 ed. Wiley; 2014.
[25] Kirby R. A comparison between analytic and numerical methods for modelling automotive dissipative silencers with mean flow. J Sound Vib 2009;325(3):565–82.
[26] Bento HFM, Ragni D, Avallone F, Simons DG, Snellen M. Acoustic wall treatments for wind tunnel aeroacoustic measurements. J Sound Vib 2018. https://doi.org/10.1016/j.jsv.2018.01.034
[27] Morganti F, Fausti P, Secchi S. On the acoustic transparency of perforated metal plates facing a porous fibrous material. Noise Mapp. 2021;8(1):191–201. https://doi.org/10.1515/noise-2021-0014
[28] Auhl RR, McLaughlin DK, Morris PJ. Design, assembly and testing of an upgraded aeroacoustics wind tunnel facility. Int J Aeroacoustics 2024;23(3–4):217–44. https://doi.org/10.1177/1475472X241230650
[29] Pott-Pollenske M, Delfs J. Enhanced capabilities of the aeroacoustic wind tunnel Braunschweig. In: 14th AIAA/CEAS aeroacoustics conference (29th AIAA aeroacoustics conference); 2008) AIAA 2008–2910.
[30] Moreau DJ, Doolan CJ. Noise-reduction mechanism of a flat-plate serrated trailing edge. AIAA J 2013;51(10):2513–22. https://doi.org/10.2514/1.J052436
[31] Pascioni K, Reger R, Edstrand A, Cattafesta L. Characterization of an aeroacoustic wind tunnel facility. In: INTERNOISE 2014 - 43rd international congress on noise control engineering: improving the world through noise control; Jan 2014.
[32] Parisot-Dupuis H, Bury Y, Barricau P, Mellot B. Characterization of ISAE-SUPAERO aeroacoustic wind tunnel. In: Forum acusticum 2023; 2023. https://doi.org/10.61782/fa.2023.1203
[33] Lylloff O, Fischer A, Fernandez-Grande E, Bak C. Acoustic design evaluation of an anechoic wind tunnel. Int J Aeroacoustics 2026;25(3–4). https://doi.org/10.1177/1475472X261419076
[34] Holthusen H, Bergmann A, Sijtsma P. Investigations and measures to improve the acoustic characteristics of the German-Dutch wind tunnel DNW-LLF. In: 18th AIAA/CEAS aeroacoustics conference (33rd AIAA aeroacoustics conference). American Institute of Aeronautics and Astronautics; 2012. p. 2176. https://doi.org/10.2514/6.2012-2176
[35] Auteri F, Belan M, Cassinelli C, Gibertini G. Interacting wakes of two normal flat plates an investigation based on phase averaging of LDA signals. J Vis 2009;12:307–21.
[36] Bradshaw P, Pankhurst RC. The design of low-speed wind tunnels. Oxford: Pergamon Press; 1976.
[37] Mehta RD. Turbulence characteristics of flow through screens and honeycombs. J Fluid Mech 1985;138:1–35. https://doi.org/10.1017/S002211208500258X
[38] Groth J, Johansson AV. Turbulence reduction by screens. J Fluid Mech 1988;197:139–55. https://doi.org/10.1017/S0022112088003209
[39] Saric WS, Reshotko E. Review of flow quality issues in wind tunnel testing. In: 2nd AIAA theoretical fluid mechanics meeting. AIAA; 1998. p. 2603. https://doi.org/10.2514/6.1998-2603
[40] AGARD Fluid Dynamics Panel Working Group. A further review of current research related to the design and operation of large windtunnels. Tech. Rep. AGARD-AR-105 Neuilly-sur-Seine, France: Advisory Group for Aerospace Research and Development (AGARD) / NATO; 1977.
[41] Jin L, Gu Y, Deng X, Sun H, Yue T, Zhang J. Standing wave and its impact on the low-frequency pressure fluctuation in an open jet wind tunnel. J Wind Eng Ind Aerodyn 2020;208:104413. https://doi.org/10.1016/j.jweia.2020.104413
[42] Mehta RD, Bradshaw P. Design rules for small low speed wind tunnels. Aeronaut J 1979;83(827):443–53. https://doi.org/10.1017/S0001924000031985
[43] Bruun HH. Hot-wire anemometry: principles and signal analysis. Oxford: Oxford University Press; 1995.
[44] Pope SB. Turbulent flows. Cambridge: Cambridge University Press; 2000.
[45] Dantec Dynamics. CTA source book. Skovlunde, Denmark, Technical guide for Constant Temperature Anemometry (Dantec Dynamics A/S; 2015. https://www.dantecdynamics.com.
[46] Crow SC, Champagne FH. Orderly structure in jet turbulence. J Fluid Mech 1971;48(3):547–91.
[47] Ho C-M, Huerre P. Perturbed free shear layers. Annu Rev Fluid Mech 1984;16(1):365–422.
[48] Schlichting H. Boundary-layer theory, McGraw-Hill Series in Mechanical Engineering. 7th ed. New York: McGraw-Hill; 1979.
[49] Görtler H. Berechnung von aufgaben der freien turbulenz auf grund eines neuen näherungsansatzes. ZAMM - Z. für Angew. Math. Mech. 1942;22(5):244–54.

[50] Sulaiman Z. Effect of open-jet shear layers on aeroacoustic wind tunnel measurements [Ph.D. thesis]. Delft, Netherlands: Delft University of Technology; 2015. https://doi.org/10.4233/uuid:2a30894f-4d92-4d2a-9e73-b3c9597143e1
[51] Ffowcs Williams JE, Hall LH. Aerodynamic sound generation by turbulent flow in the vicinity of a scattering half-plane. J Fluid Mech 1970;40(4):657–70.
[52] Brooks TF, Hodgson TH. Prediction and comparison of jet-surface interaction noise. J Sound Vib 1981;78(1):79–112.
[53] Lighthill MJ. On sound generated aerodynamically. I. general theory. Proc. R. Soc. Lond. A. Math. Phys. Sci. 1952;211(1107):564–87.
[54] Amiet RK. Correction of open jet wind tunnel measurements for shear layer refraction. In: 2nd aeroacoustics conference. Hampton, VA, U.S.A.: AIAA; 1975, AIAA Paper 75-532. https://doi.org/10.2514/6.1975-532
[55] Plumblee HE, Dean PD, Wynne GA, Burrin RH. Sound propagation in and radiation from acoustically lined flow ducts: a phenomenological study of sound propagation through a free shear layer. Tech. Rep. NASA CR-2702 Washington, D.C.: National Aeronautics and Space Administration; Jul 1976.
[56] Schlichting H, Gersten K. Boundary-layer theory. 9 ed. Berlin: Springer; 1997.
[57] Geyer TF, Sarradj E. Circular cylinders with soft porous cover for flow noise reduction. Exp Fluids 2016;57:30. https://doi.org/10.1007/s00348-016-2119-7
[58] Brooks TF, Pope DS, Marcolini MA. Airfoil self-noise and prediction. Technical Report, NASA Technical Report Hampton, Virginia, United States: NASA Langley Research Center; 1989.